Epilepsy-linked kinase CDKL5 phosphorylates voltage-gated calcium channel Cav2.3, altering inactivation kinetics and neuronal excitability

Marisol Sampedro-Castañeda[1,5,*], Lucas L. Baltussen[1,4,5], Andre T. Lopes[1], Yichen Qiu[2], Liina Sirvio[1], Simeon R. Mihaylov[1], Suzanne Claxton[1], Jill C. Richardson[3], Gabriele Lignani[2], Sila K. Ultanir[1]*

1. Kinases and Brain Development Lab, The Francis Crick Institute, 1 Midland Road, London NW1 1AT, United Kingdom

2. Department of Clinical and Experimental Epilepsy, UCL Queen Square Institute of Neurology, 808 Queen Square House, London WC1N 3BG, United Kingdom

3. UK Neuroscience Group, MSD R&D Innovation Centre, 120 Moorgate, London, EC2M 6UR, United Kingdom

* Correspondence: sila.ultanir@crick.ac.uk, marisol.sampedro-castaneda@crick.ac.uk

4. Current address: Laboratory of Synapse Biology (VIB-KU Leuven), Department of Neurosciences, ON5 Herestraat 49, 3000 Leuven, Belgium

5. These authors contributed equally

Abstract

Developmental and epileptic encephalopathies (DEEs) are a group of rare childhood disorders characterized by severe epilepsy and cognitive deficits. Numerous DEE genes have been discovered thanks to advances in genomic diagnosis, yet putative molecular links between these disorders are unknown. CDKL5 deficiency disorder (CDD, DEE2), one of the most common genetic epilepsies, is caused by loss-of-function mutations in the brain-enriched kinase CDKL5. To elucidate CDKL5 function, we looked for CDKL5 substrates using a SILAC-based phosphoproteomic screen. We identified the voltage-gated Ca^{2+} channel Cav2.3 (encoded by *CACNA1E*) as a novel physiological target of CDKL5 in mice and humans. Recombinant channel electrophysiology and interdisciplinary characterization of Cav2.3 phosphomutant mice revealed that loss of Cav2.3 phosphorylation leads to channel gain-of-function via slower inactivation and enhanced cholinergic stimulation, resulting in increased neuronal excitability. Our results thus show that CDD is partly a channelopathy. The properties of unphosphorylated Cav2.3 closely resemble those described for *CACNA1E* gain-of-function mutations causing DEE69, a disorder sharing clinical features with CDD. We show that these two single-gene diseases are mechanistically related and could be ameliorated with Cav2.3 inhibitors.

Keywords

CDKL5, CACNA1E, Cav2.3, epilepsy, developmental and epileptic encephalopathy, DEE2, DEE69

48 **Introduction**

49 Developmental and epileptic encephalopathies (DEE) are characterized by severe early-onset
50 epileptic activity accompanied by global developmental and cognitive impairments. The
51 genetic aetiology approximately 90 DEEs has been identified [1], but targeted therapies remain
52 scarce. Elucidating shared pathways in infantile-onset epilepsies will reveal molecular links
53 between disease genes and greatly advance common targeted treatments.

54

55 Cyclin dependent kinase like-5 (CDKL5) is a brain-enriched serine-threonine kinase. *De novo*
56 loss-of-function mutations in the X-linked *CDKL5* gene, including missense, nonsense and
57 insertions/deletions, cause CDKL5 deficiency disorder (CDD) (OMIM 300672, 300203) [2, 3, 4, 5].
58 Pathogenic missense mutations, almost exclusively located in the kinase domain, indicate that
59 kinase activity is critical for CDD pathology [6, 7, 8, 9]. CDD is characterized by infantile-onset,
60 intractable seizures, profound neurodevelopmental impairment in motor and sensory function,
61 impaired language acquisition and autonomic disturbances [3, 5]. The estimated incidence for
62 CDD is 1/42,000 live births each year [10, 11, 12] with approximately 80% being female patients,
63 making it one of the most common types of genetic childhood epilepsy [13, 14].

64 CDKL5 is highly enriched throughout the forebrain with expression starting at late embryonic
65 stages in rodents and humans [15, 16, 17, 18, 19]. Low levels of expression were reported in other
66 tissues [16]. Phosphorylation targets include microtubule binding proteins EB2 and MAP1S [6, 20]
67 and transcriptional regulators ELOA [21] and Sox9 [22], showing its diverse cellular roles. CDKL5
68 knockout (KO) neurons have deficits in synaptic transmission, dendritic spine development,
69 neurite outgrowth, cilia elongation and microtubule dynamics [23, 24, 25, 26, 27, 28, 29]. However,
70 molecular mechanisms linking CDKL5 loss to neuronal hyperexcitability remain unknown. The
71 identification of key physiological targets of CDKL5 directly involved in the regulation of cellular
72 excitability may help elucidate epileptogenic mechanisms and lead to effective therapies.

73 Voltage-gated calcium channels (VGCC) have a key role in physiology, driving neuronal
74 excitability and allowing influx of second messenger Ca^{2+} ions in response to membrane

depolarization [30, 31, 32]. VGCC subtype Cav2.3 is formed by the ion-conducting α1E subunit (encoded by *CACNA1E*) in complex with accessory subunits from the β and α2δ families. Cav2.3 is highly expressed in the CNS, where it is localized at both pre- and post-synaptic sites in neurons, as shown functionally and by immuno-EM [33, 34, 35]. *CACNA1E* knockout mice demonstrated that Cav2.3 mediates neuronal R-type Ca^{+2} currents [35, 36, 37], so-called due to their "resistance" to organic VGCC channel inhibitors [38, 39]. Cav2.3 is dynamically regulated by phosphorylation at multiple sites [40, 41]. In general, VGCC phosphorylation is an important mechanism by which neuromodulators and their G-protein coupled receptors (GPCRs) exert their effect on cellular excitability [42].

De novo heterozygous missense mutations in *CACNA1E* cause an infantile epileptic encephalopathy (OMIM 618285) [43, 44]. Cav2.3 variants studied *in vitro* have altered gating and/or inactivation kinetics, leading to gain-of-function (GoF) of Cav2.3 [43, 44]. Patients with *CACNA1E* mutations have overlapping clinical phenotypes with CDD, such as intractable seizures, profound intellectual disability and hypotonia. Single-gene DEEs such as this one are estimated to impact approximately 1/2100 live births [10], but their real prevalence is unknown as more genes are being identified rapidly due to recent advances in genetic diagnosis [45, 46]. Despite, overlapping clinical features, potential molecular links between these rare disorders remain to be elucidated.

In this work, we apply for the first time a global phosphoproteomics approach in CDKL5 knockout mice and identify and validate Cav2.3 as a novel substrate of CDKL5 in human and mouse neurons. Through our analysis of Cav2.3 function and characterization of a novel Cav2.3 phosphomutant mouse line, in which CDKL5 phosphorylation site is mutated, we reveal that lack of phosphorylation leads to Cav2.3 gain-of-function and hyperexcitability. Our results indicate that developmental and epileptic encephalopathies caused by *CDKL5* and

101 *CACNA1E* are related at the molecular level. We propose Cav2.3 as a converging therapeutic
102 target for these disorders.
103

104 **Results**

105 **Cav2.3 is a CDKL5 phosphorylation substrate in mice and humans**

106 We used stable isotope labelling of amino acids in cell culture (SILAC) [47] to differentially tag
107 newly synthesized proteins in primary cortical cultures from wild type (WT) and CDKL5
108 knockout (KO) mice [48] and compare changes in protein phosphorylation levels (Fig. 1a). As
109 expected in CDKL5 KO neurons, we observe a significant reduction in CDKL5 pS407 and in
110 EB2 pS222, a known CDKL5 phosphorylation target [20]. Phosphorylation of EB2 S221 was
111 also decreased, indicating co-regulation of these neighbouring sites. More importantly, a
112 potential new target protein, the ion channel Cav2.3, showed strongly reduced
113 phosphorylation at S15 (pS15), in CDKL5 KO neurons. Strikingly, the Cav2.3 S15 site matches
114 the RPXS/T* consensus motif [6, 20], suggesting direct CDKL5 phosphorylation (Fig. 1a, b). S15,
115 located in the N-terminus of the α1E channel pore subunit (Fig. 1b), is conserved in humans
116 (S14) but absent in the related Cav2.1 (*CACNA1A*) and Cav2.2 (*CACNA1B*) channels (Fig.
117 1b).

118 To test if CDKL5 can phosphorylate Cav2.3 S15, we generated a phosphospecific antibody
119 targeting this site. Overexpression of Cav2.3 (& ancillary subunits) together with the CDKL5
120 kinase domain in HEK293 cells shows strong Cav2.3 phosphorylation *in vitro* (Cav2.3 pS14,
121 Fig. 1c, f). This phosphorylation is absent when overexpressing phosphomutant Cav2.3 or
122 kinase-dead CDKL5, demonstrating the specificity of the antibody and the dependence of
123 phosphorylation at this site on CDKL5 kinase activity. Importantly, full-length CDKL5 also
124 directly phosphorylated Cav2.3 *in vitro* (Supplementary Fig. 1a, b). Cav2.3 phosphorylation is
125 consistently reduced in the cortex of CDKL5 KO mice at postnatal day P20 (Cav2.3 pS15),
126 validating the substrate *in vivo* (Fig. 1d, g). Finally, Cav2.3 pS14 was decreased in human

127 iPSC-derived neurons from CDD patients (Fig. 1e, h), demonstrating altered phospho-
128 regulation of this target in CDD. Together, these results show that Cav2.3 is a *bona fide*
129 CDKL5 phosphorylation target in mice and humans.

130 **Loss of Cav2.3 Ser14 phosphorylation slows baseline channel kinetics and amplifies**
131 **muscarinic regulation**

132 Cav2.3 is causally linked to epilepsy by two main lines of evidence. First, channel deletion
133 renders mice resistant to tonic-clonic seizures [49, 50, 51]. On the other hand, Cav2.3 GoF leads
134 to severe epileptic encephalopathy in humans [43, 44]. The remarkable overlap in clinical
135 manifestations between CACNA1E and CDD patients, including seizures and
136 neurodevelopmental delays, raises the possibility that Cav2.3 regulation by CDKL5 might
137 affect channel function and in turn neuronal excitability.

138 To test the effect of pS14 on Cav2.3 channel properties we used a HEK293 cell line stably
139 expressing the human auxiliary subunits β3 and α2δ1 and transiently transfected human α1E
140 and full-length CDKL5 plasmids (Supplementary Fig. 1a, b). Whole-cell patch-clamp
141 recordings of Cav2.3 Ba^{2+} currents revealed slower decay kinetics (inactivation τ) in S14A
142 mutant channels (Fig. 2a-c). Notably, in absence of CDKL5, WT Cav2.3 decay kinetics were
143 indistinguishable from S14A Cav2.3 mutant (Fig. 2d). We also found a statistically significant
144 increase in whole-cell current density at maximum activation voltages in S14A when compared
145 to WT Cav2.3 in presence of CDKL5 (Fig. 2e). To account for differences in biophysical
146 properties that may be introduced by α1E association with a different β subunit [52, 53], we
147 conducted parallel experiments in a HEK293 cell line stably expressing human α2δ1 and β1b,
148 another Cavβ subunit associated with α1E in the brain [54]. We used Ca^{2+} as charge carrier to
149 examine channel properties in a more physiological context. Decay kinetics of WT Cav2.3
150 currents with β1b were substantially slower than currents with β3 (Supplementary Fig. 2 a, b
151 *vs.* Fig 1a, b), as previously reported [52]. In absence of CDKL5 phosphorylation (S14A α1E
152 mutant or kinase-dead CDKL5 conditions), Cav2.3 current inactivation was further slowed

153 (Supplementary Fig. 2a-c), recapitulating our results with β3 (Fig. 2a-c). Current density at
154 maximal activation voltages did not reach significance in the β1-expressing cells, where
155 currents were generally larger (Supplementary Fig. 2d). Finally, we observed no changes in
156 half maximal activation and inactivation potential or time course of recovery from fast
157 inactivation in β3- or β1-expressing cells (Fig. 2f and Supplementary 2e,f).

158 Altogether, our results indicate that CDKL5-mediated Ser14 phosphorylation of α1E speeds
159 up the inactivation of human Cav2.3 and suppresses current amplitude, independent of Cavβ
160 subtype or charge carrier. Consequently, absence of CDKL5 leads to Cav2.3 GoF, with larger
161 and more prolonged currents. A subset of *CACNA1E* GoF mutations described in human DEE
162 patients also cause slower inactivation kinetics and/or increased current density [43], mirroring
163 the phenotypes observed in the unphosphorylated channel. Thus, the functional deficits in
164 Cav2.3 observed in absence of CDKL5 phosphorylation match those caused by pathological
165 point mutations in Cav2.3 and could partly explain the pathophysiology of CDD.

166 Cav2.3 channels are downstream targets of muscarinic acetylcholine receptors, which modify
167 channel function predominantly via PKC-mediated phosphorylation, leading to current
168 enhancement in HEK293 cells and neurons [55, 56, 57]. Given the observed GoF in S14A Cav2.3,
169 we hypothesized that muscarinic receptor enhancement may also be affected by CDKL5
170 phosphorylation. To test this, we co-expressed Cav2.3, CDKL5 and muscarinic acetylcholine
171 receptor type 3 or 1 (M3 or M1), which are prominent brain subtypes known to regulate
172 neuronal Cav2.3 post-synaptically. As expected, application of the non-hydrolysable agonist
173 carbachol substantially increased current amplitude regardless of Ser14 phosphorylation in
174 both β3 and β1 stable cell lines (Fig. 2g-l). The current increase with carbachol was 1.5 to 2
175 fold greater in cells without phospho-Ser14 at -10 mV (Fig. 2g, h, j, l), reflecting Cav2.3 gain-
176 of-function in absence of phosphorylation. The half-maximal activation potential ($V_{1/2}$) was left-
177 shifted by 5 mV for WT channels in both cell lines, a described effect of muscarinic receptor
178 activation [56, 58]. Interestingly, without Ser14 phosphorylation this shift was significantly greater,
179 implying an effect of phospho-Ser14 on the modulation of Cav2.3 gating (Fig. 2m-p). This

180 represents an additional gain-of-function due to loss of CDKL5, a phenotype comparable to
181 pathogenic *CACNA1E* mutations that alter $V_{1/2}$ [43].

182 Upon GPCR activation, Cav2.3 channels can be suppressed by $G_{\beta\gamma}$ subunits. This effect is
183 has been observed in Gαq-coupled receptors including M1/M3 in HEK293 cells [56] and CA1
184 neurons [55]. The Cav2.3 N-terminus and Cavβ are involved in $G_{\beta\gamma}$ regulation [59, 60]. For this
185 reason, we investigated the possibility that the enhanced carbachol effects in absence of N-
186 terminal pS14 could be due to reduced $G_{\beta\gamma}$ suppression. To distinguish between PKC-
187 mediated enhancement and $G_{\beta\gamma}$ suppression, we boosted PKC activity prior to carbachol
188 application using phorbol 12-myristate 13-acetate (PMA), reliably increasing Cav2.3 currents
189 [56, 61]. With further addition of carbachol we found no evidence of muscarinic inhibition of human
190 WT Cav2.3 channels (Supplementary Fig. 2g, h). Moreover, co-expression of Cav2.3 and Gi-
191 coupled dopamine D2 receptors to further probe $G_{\beta\gamma}$ inhibition in our system, revealed
192 significant reduction in peak currents upon D2 activation with quinpirole [59]. However, there
193 was no difference in inhibitory modulation with or without Ser14 phosphorylation
194 (Supplementary Fig. 2i, j). The above manipulations suggest that $G_{\beta\gamma}$ is not involved in
195 pathological Cav2.3 GoF.

196 Our results describe two Cav2.3 gain-of-function (GoF) mechanisms in the absence of CDKL5
197 phosphorylation: slower decay kinetics and a left shift in voltage-dependence of activation
198 ($V_{1/2}$) upon muscarinic activation, both reflected in increased Ca^{2+} influx through Cav2.3
199 channels. These GoF features are reminiscent of those described for pathological Cav2.3
200 variants.

201 **Altered R-type current inactivation and increased excitability in neurons from Cav2.3**
202 **S15A phosphomutant mice**

203 To investigate the role of Cav2.3 S15 phosphorylation in neurons, we generated Cav2.3 S15A
204 phosphomutant mice using CRISPR-Cas9 genome editing. We found that the total S15
205 phosphorylation levels detected by our phosphoantibody were reduced to <20% of control

206 levels in homozygous S15A mice (HOM S15A) while total Cav2.3 levels were not changed
207 (Fig. 3a-c). Cav2.3 is highly expressed in the somato-dendritic region of CA1 hippocampal
208 neurons [34] where it underlies most of the R-type current and regulates intrinsic excitability [35,
209 55]. We performed whole-cell somatic recordings in acute slices from young mice and recorded
210 pharmacologically isolated Cav2.3 Ca^{2+} currents in these cells. When compared to wild type
211 littermates (WT), HOM S15A mice showed significantly slower inactivation τ at maximal
212 conductance voltages, recapitulating HEK293 cell results (Fig. 3 d, e). Current amplitudes at
213 the soma did not differ (Fig. 3f).

214 We next tested the effect of Cav2.3 S15A on neuronal excitability and cholinergic
215 neuromodulation in response to depolarising current injections in adult CA1 pyramidal cells.
216 Resting membrane potential (V_{rest}), input resistance (R_{in}) and firing properties were identical
217 between WT and S15A mice under baseline conditions (Fig. 3g-i). Following bath application
218 of carbachol, we observed a 4 mV depolarisation in V_{rest} and a 25% increase in R_{in} (Fig 3g),
219 changes that were comparable between WT and S15A neurons (Supplementary Fig. 3a).
220 These alterations are likely due to conductances other than Cav2.3, in line with previous
221 reports [58, 62, 63].

222 In neurons, cholinergic activation can elicit sustained depolarizing plateau potentials (DPPs):
223 all-or-none, large amplitude depolarizations that outlast stimulus-evoked firing [58, 64, 65]. A
224 muscarinic medium duration afterdepolarization (ADP) is also reported in CA1 pyramidal cells
225 [66]. Up-regulation of Cav2.3-mediated R-type currents is required for DPPs and ADPs in
226 hippocampus [67] and cortex [65]. We inspected these Cav2.3-dependent hyper-excitability
227 measures in S15A mice. Carbachol application significantly increased action potential firing
228 frequency in WT and S15A neurons (Fig. 3 h-k). At current injections greater than 250 pA,
229 however, phosphomutant neurons responded with fewer spikes and depolarization block
230 towards the end of the stimulus step, indicating greater underlying depolarization. The
231 percentage of cells exhibiting at least one DPP or all-or-none afterdepolarization (ADP) >8 mV
232 upon carbachol treatment was significantly higher in S15A mice, showing an enhanced

233 depolarization response (Fig. 3j, k). Importantly, the occurrence of DPP/large ADPs was
234 shifted towards lower current injections in S15A cells (Fig. 3l). Greater perisomatic
235 depolarization in S15A neurons was also reflected in a larger ADP at 100ms post stimulus and
236 more spike attenuation (Supplementary Fig. 3b, c). Together with the enhanced carbachol-
237 mediated left-shift in $V_{1/2}$ observed in phosphomutant channels in HEK293 cells (Fig. 2 j,l),
238 these increased neuronal depolarizations in Cav2.3 phosphomutant mice suggest facilitation
239 of gating of endogenous Cav2.3 without S15 phosphorylation upon cholinergic agonist
240 application.

241 We tested if other conductances known to be regulated by carbachol are altered in Cav2.3
242 phosphomutants. The medium- and slow-afterhyperpolarizations (AHPs) are critical for spike
243 frequency regulation and their underlying K^+ and mixed-cationic currents are targets of the
244 muscarinic system [62, 68, 69]. Baseline AHPs elicited by a short spike burst were not different
245 between WT and S15A mice and were equally suppressed by carbachol application
246 (Supplementary Fig. 3d). We also analysed baseline small-conductance Ca^{2+}-activated K^+
247 (SK) currents and spontaneous excitatory synaptic currents (EPSCs), known to be functionally
248 coupled to [70] or modulated by [71] Cav2.3 in CA1 neurons. We hypothesized that these may be
249 affected given the prolonged Cav2.3 currents in S15A mice, but our measurements show no
250 differences between genotypes (Supplementary Fig. 3e-h). Therefore, we suggest that the
251 increased carbachol-induced excitability of CA1 neurons in Cav2.3 S15A knock-in mice is
252 specifically due to Cav2.3 GoF.

253 **Cav2.3 S15A phosphomutant mice have behavioural and EEG deficits**

254 Multiple CDKL5 KO mouse models have been generated by deleting exons 4, 2 or 6, all of
255 which led to loss of CDKL5 protein [15, 18, 48]. Numerous behavioural deficits were reported in
256 CDKL5 KO mice [15, 48, 72, 73, 74], thus we investigated behavioural phenotypes in Cav2.3 S15A
257 phosphomutant mice to see if any of the CDKL5 KO impairments are recapitulated. We
258 observed no spontaneous behavioural seizures in Cav2.3 S15A, as reported for CDKL5 KO
259 mice [15, 18, 48], but see [75, 76]. When monitored in a home-cage environment for prolonged periods,

260 S15A showed reduced locomotion and voluntary wheel use (Fig. 4a, b), also observed in
261 CDKL5 KO mice [48]. We observed minor changes in locomotion and zone preference in the
262 open field test, but only towards the end of a 30 min trial (Supplementary Fig. 4c, 4a),
263 potentially indicating fatigue rather than anxiety. Unlike CDKL5 KOs, S15A mice did not
264 present hindlimb clasping (mean scores: WT 0.041, HOM S15A 0, p=0.334, unpaired t test)
265 and performed equally in the rotarod test (Fig. 4d) when compared to WT littermates. Cognitive
266 abilities in the Y- and Barnes maze were also unchanged in phosphomutants (Supplementary
267 Fig. 4b-e). On the other hand, S15A mice had mild impairments in sociability (Fig. 4e). A
268 consistently reported phenotype of CDKL5 KO mice is altered contextual fear conditioning
269 responses [15, 73]. Memory formation, retention and extinction in this task were also defective in
270 Cav2.3 S15A (Fig. 4f), indicating a clear overlap with CDKL5 KOs.

271 Finally, given the high epilepsy incidence in human CDKL5 and CACNA1E DEE patients,
272 seizure susceptibility was analysed in a separate cohort using wireless electrocorticogram
273 (ECoG) transmitters [77] and repeated low-dose kainic-acid (KA) injections [78] (Fig. 4g-i). We
274 found no changes in baseline ECoG (Fig 4g) or overall KA-induced seizure susceptibility in
275 S15A mice (Fig. 4h), similar to KA-induced seizures in CDKL5 KO mice [18, 48]. Interestingly,
276 however, female S15A mice had a reduced threshold to stage 5 behavioural seizures with an
277 increase in ECoG activity during KA (Fig. 4h,i).

278 In summary, our *in vivo* analyses of Cav2.3 S15A mice demonstrate similarities with CDD
279 mouse models and patients, including social, motor and cognitive impairments, and to some
280 extent increased seizure susceptibility. These observations suggest that loss of pS15 is a key
281 contributor to the phenotypic features of CDD.

282

283 **Discussion**

284 There are currently no disease-targeting therapies for CDD and the causes of aberrant
285 excitability in absence of CDKL5 are unknown. Here we identify the alpha subunit of Cav2.3

286 channel complex as a CDKL5 phosphorylation substrate in mouse and human neurons.
287 *CACNA1E* mutations cause severe early onset epilepsy in humans and there is remarkable
288 overlap between CDD and patients with *CACNA1E* mutations. These include intractable
289 seizures, global developmental delay, intellectual disability, hypotonia, hyperkinetic
290 movements and sleep disturbances. A consistent feature of Cav2.3 variants associated with
291 epilepsy is GoF of the channel, by left-shifting the activation voltage, altering maximal current
292 and/or by slowing inactivation [43]. Our data shows that deletion of CDKL5 results in loss of
293 Cav2.3 S15 phosphorylation, leading to GoF due to slowed inactivation and amplified gating
294 modulation, similar to the effects observed in Cav2.3 variants. Our results establish Cav2.3
295 overactivity as a common feature of CACNA1E (DEE69) and CDKL5 (DEE2) epileptic
296 encephalopathies, potentially explaining overlapping clinical features of these diseases.

297 Cytoplasmic N-terminal S15 phosphorylation of Cav2.3 has been previously detected in global
298 phosphoproteomics screens from brain (phosphosite.org), but the responsible kinase and the
299 role of this phosphorylation were unknown. N-terminal deletions in Cav2.3 [59] or the related
300 Cav2.2 [79, 80], result in channels with normal gating and conduction properties. Inactivation
301 kinetics were not measured in these studies, yet interestingly Cav2.2 N-terminal deletion
302 mutants seemed to have slower decaying currents, indicating that this region participates in
303 the regulation of inactivation [79]. Analogously, loss of N-terminal Ser14/15 phosphorylation
304 slows Cav2.3 inactivation in HEK293 cells and neurons, underscoring a previously overlooked
305 regulatory role of the Cav2.3 N-terminus. This domain may interact with Cavβ, as previously
306 suggested for Cav2.2 [80].

307 We also find that cholinergic stimulation amplifies Cav2.3 GoF in absence of CDKL5
308 phosphorylation, by prominently shifting activation $V_{1/2}$ and increasing currents at maximal
309 activation voltages, thus revealing a second molecular mechanism by which loss of pS14/15
310 enhances Cav2.3 function. It is known that muscarinic enhancement of Cav2.3 depends on
311 Gαq signalling and PKC phosphorylation at multiple sites, including the intracellular loop I-II
312 [61], the most prominent site of α1-β interaction [53]. We show that loss of pS14 interferes with

313 PKC enhancement upon carbachol application, but the mechanisms of this interplay are yet
314 to be established.

315 Our recordings from hippocampal neurons in Cav2.3 S15A mice demonstrate that S15
316 regulates Cav2.3 function in neurons. We show that pS15 is critical for R-type current
317 inactivation and regulation of firing by cholinergic stimulation. Isolating Cav2.3 currents is
318 challenging due to space clamp limitations and the need for inhibitors of other voltage-gated
319 channels. These drugs may have promiscuous effects on Cav2.3 [81] or incompletely block other
320 Ca^{2+} currents [55]. We observed enhanced neuronal excitability and increased pro-epileptiform
321 cholinergic ADPs/DPPs [58, 63] in Cav2.3 phosphomutant mice, an effect that was not linked to
322 carbachol suppression of AHPs or other intrinsic excitability properties in these cells. Instead,
323 we suggest that the GoF of unphosphorylated Cav2.3 underlies the hyper-excitability seen in
324 response to muscarinic stimulation. Interestingly, CDKL5 KO mice have altered cholinergic
325 tone [82] and the muscarinic antagonist Solifenacin was shown to ameliorate network defects in
326 CDD patient-derived neurons [83], supporting an enhanced cholinergic modulation in this human
327 model.

328 We find striking behavioural similarities between our Cav2.3 phosphomutant mice and CDKL5
329 KOs. Specifically, S15A mice show reduced encoding and retention of fear memory, a robust
330 phenotype found in full body [15, 73, 84] and excitatory neuron-specific [85] CDKL5 KO mice. Cav2.3
331 KO mice display enhanced contextual fear conditioning [37]. Cav2.3 S15A mice recapitulate the
332 reduced home-cage locomotion behaviour in CDKL5 KO mice [48, 73]. The deficits observed in
333 voluntary wheel in Cav2.3 phosphomutants could be indicative of mild hypotonia [86, 87]. Finally,
334 reduced social interaction in Cav2.3 phosphomutant mice was also observed in CDKL5 KO
335 mice [15, 48, 73] and inhibitory neuron specific deletion of CDKL5 [88]. Importantly, these
336 phosphomutant mouse phenotypes mirror human clinical manifestations of CDD, arguing that
337 slowed inactivation and enhanced cholinergic modulation of unphosphorylated Cav2.3 may
338 contribute to these symptoms.

339 Cav2.3 KO mice exhibit reduced susceptibility to chemical absence seizures [89, 90, 91] and
340 hippocampal KA-induced seizures [51]. In agreement with Cav2.3's role in epilepsy, we find
341 increased seizure susceptibility in females in the low-dose KA injection paradigm in our Cav2.3
342 S15A mice. The difference between males and females, observed in both ECoG and
343 behavioural seizure analysis, may arise from increased basal function of Cav2.3 in the female
344 brain downstream of hormonal signals. Therefore, gender should be taken into consideration
345 in future mouse CDKL5 KO studies, where seizure susceptibility has not been observed in
346 one gender. In CDKL5 KO males, KA-induced seizure susceptibility changes have not been
347 observed [18, 48]. Reduced latency to seizure initiation with pentylenetetrazole (PTZ, a $GABA_A$
348 receptor inhibitor) injections has been reported in CDKL5 KO males [84] as well as heterozygous
349 females [74]. Finally, increased severity of seizures upon NMDA injections were observed in
350 male CDKL5 KO mice due to increase NMDAR function [18], however NMDAR function is not
351 altered in CDKL5 KO rats [29]. In absence of pro-convulsants, disturbance-associated seizures
352 are observed only in aged heterozygous females in two different CDD mouse models [75], an
353 occurrence that may be linked to developmental changes in Cav2.3 regulation.

354 In rodents, it is possible to reverse adult phenotypes with reintroduction of CDKL5 genetically
355 [72] or using AAV viruses [92], indicating an open therapeutic window for treatment. Here, we
356 report a novel functional regulation of Cav2.3 by CDKL5 phosphorylation, which impinges of
357 neuronal excitability. Thus Cav2.3 GoF in absence of CDKL5 may be an important molecular
358 mechanism in CDD pathology. In addition to CDKL5 and CACNA1E encephalopathies,
359 increased Ca^{2+} influx through Cav2.3 may contribute to seizures in Fragile X syndrome, as
360 reduced FMRP function leads to increased Cav2.3 expression [93]. Cav2.3 also increases
361 susceptibility to drug-induced Parkinson's disease [95, 96]. We propose that Cav2.3 inhibitors/
362 modulators could be beneficial for CDD patients and potentially for a broader population of
363 neurological patients in the future.

364

365

366 ## Methods

367 ### Mouse handling and mutant generation

368 Animals were housed in a controlled environment with 12-hour light/dark cycle. They were fed
369 *ad libitum* and used in accordance with the principles of the "3Rs" and the Animals (Scientific
370 Procedures) Act 1986 of the United Kingdom. Protocols and procedures were approved by
371 The Francis Crick Institute and UCL Institute of Neurology oversight committees. Except for
372 some *in vivo* experiments, mice were housed in groups. Mouse strains were backcrossed into
373 C57 Bl/6 (Jackson) and none of the experimental mice were immunocompromised. Male and
374 female mice aged embryonic day (E)16.5 to postnatal 30 weeks were used as specified.

375 CDKL5 KO animals were a kind gift from Cornelius Gross [48]. Mutant Cav2.3 Ser15Ala animals
376 were created in-house using the CRISPR/Cas9 system. The guide contained the sequence
377 5'AGGCUCAGGCGAUGGAGACU3'. This replaced the original DNA sequence of 5'
378 AGGCGCAGGCGATGGAGACT 3' in CACNA1E. Genetically altered C57Bl6 embryos were
379 obtained using electroporation as part of Francis Crick Institute's Genetic Modification
380 Services. Genotype was determined by in-house PCR or Sanger sequencing (Source
381 Bioscience).

382 ### SILAC phosphoproteomics

383 Sample preparation

384 Mouse cortical neurons were cultured from individual male E16.5 embryos from a
385 heterozygous Cdkl5 female. Cdkl5 +/Y (WT) or -/Y (KO) genotype of embryos was determined
386 afterwards. Neurons were plated at a density of 8x10^6 cells per 10 cm dish coated with 60
387 µg/ml poly-D-lysine (Sigma) and 2.5 µg/ml laminin (Sigma). Cells were grown in neurobasal
388 media free of L-Arginine and L-Lysine (Invitrogen) supplied with either Lysine 8 (U-13C6, U-
389 15N2) and Arginine 10 (U-13C6, U-15N4) or Lysine 4 (4, 4, 5, 5-D4) and Arginine 6 (U-13C6).
390 L-Proline (200mg/ml) was supplemented to prevent Arginine to Proline conversion. At DIV4,

391 1 μM Ara-C was added to inhibit glia growth. For every embryo, one dish was labelled with
392 K8R10 (heavy) and one dish was labelled with K4R6 (light).

393 At DIV12, SILAC labelled primary neurons from 3 Cdkl5 WT and 3 Cdkl5 KO animals were
394 lysed in lysis buffer containing 20 mM Tris pH7.5, 100 mM NaCl, 10 mM $MgCl_2$, 0.25% IGEPAL
395 NP40, 0.5 mM DTT, 1x Protease Inhibitor Cocktail, 1 μM Okadaic Acid. Each sample was
396 checked for SILAC label incorporation and Arginine to Proline conversion. Lysates were mixed
397 to obtain 3x heavy WT/light KO and 3x heavy KO/light WT samples containing 1 mg total
398 protein. Proteins were digested overnight with Sequencing Grade Modified Trypsin/Lys-C
399 (Promega) at 37^0C, desalted using Sep-Pak Classic C18 Cartridges (Waters) and vacuum
400 dried completely. Samples were enriched for phosphopeptides using Titansphere titanium
401 dioxide beads (GL Science) in batch mode with the following buffers: Loading buffer: 80%
402 ACN, 5% TFA, 1M Glycolic Acid, Wash buffer 1: 80% ACN 1% TFA, Wash buffer 2: 10% ACN,
403 0.2% TFA, Elution buffer 1: 1% Ammonium Hydroxide, Elution buffer 2: 5% Ammonium
404 Hydroxide. Phosphopeptides were cleaned up using C18 Stage Tips with a centrifuge protocol
405 and vacuum dried completely. Samples were stored at -80^0C until required for analysis by
406 mass spectrometry.

407 Mass spectrometry

408 Each sample was resuspended in 35 μl 1% TFA, sonicated for 15 minutes and injected 3 times
409 (10 μl per injection). Peptide mixtures were separated on a 50 cm, 75 μm I.D. Pepmap column
410 over a 3 hr gradient and eluted directly into the mass spectrometer (Orbitrap Velos). Xcalibur
411 software was used to control data acquisition. The instrument ran in data dependent
412 acquisition mode with the top 10 most abundant peptides selected for MS/MS by CID, MSA
413 or HCD fragmentation techniques (one fragmentation technique per replicate).

414 Data processing was performed using the MaxQuant bioinformatics suite (v 1.3.0.5) and
415 protein database searching was done by the Andromeda search engine using a Uniprot
416 database of *Mus musculus* proteins amended with common contaminants. Default search

417 settings were used including an FDR of 1% on the phosphosite, peptide and protein level and
418 matching between runs for peptide identification. K4R6 and K8R10 were set as labels with a
419 maximum of 3 labeled AAs. Phosphorylation at serine, threonine or tyrosine residues,
420 oxidation (Met) and protein N-terminal acetylation were set as variable modifications.
421 Carbamidomethylation of Cys-residues was set as a fixed modification.

422 Data was further processed in Perseus v.1.6.15.0. Phospho (STY) sites from the six
423 experimental samples in the MaxQuant search were loaded and site tables expanded.
424 Potential contaminants and reversed hits were removed. Normalized H/L ratios were log2
425 transformed and filtered for rows containing at least three valid values. Potential CDKL5
426 substrates were annotated using the R-P-X-pS/pT motif [20]. A one-sample t-test was performed
427 comparing the normalized ratios to the null hypothesis and visualized as a volcano plot.

428 **Mutagenesis**

429 Point mutations were introduced using QuickChange site-directed mutagenesis (Agilent).
430 Complimentary primers contained the desired mutations flanked by at least 18 bp. To ensure
431 mutagenesis efficiency for each construct, two separate PCR reactions with each primer were
432 set up: 0.2 µM primer, 100 ng template DNA, 0.2 mM dNTP mix, 1x Pfu buffer and 2.5 U Pfu
433 Ultra HF. The PCR programme was run 4x, after which complementary samples were
434 combined and the PCR run repeated 20x. PCR products were treated with DpnI for 1hr at
435 37^0C and transformed into XL-10 Gold competent cells. At least 4 colonies were used for each
436 DNA miniprep (QIAprep, Qiagen) and mutations were confirmed by Sanger sequencing
437 (Source Bioscience). The constructs used were as follow: 1) HA-tagged human α1E subunit
438 (gene bank L27745.2, gift from L. Parent, Université de Montréal), in a commercial vector
439 under control of CMV promoter [97]. 2) The N-terminal FLAG-tagged full-length human $CDKL5_{107}$
440 and N-terminal HA-tagged human $CDKL5_{1-352}$ kinase domain construct kinase as previously
441 described [20].

442

443 **Cell line maintenance and transfection**

444 Tetracycline-inducible HEK293 cells expressing human Cavβ3 and α2δ1 subunits were
445 obtained from SB Drug Discovery (Glasgow, UK). HEK293 cells stably expressing human Cav
446 β1b and α2δ1 subunits were kindly provided by Andrew Powell (GSK Ltd., Middlesex, UK).
447 Naïve HEK293T cells were supplied by Francis Crick Institute's Cell Services.

448 All cells were cultured in high glucose DMEM with 10% Fetal Bovine Serum (tetracycline free,
449 Clontech or Gibco) and penicillin/streptomycin 50units/ml-50 mg/ml. They were passaged
450 using TrypLE Express and maintained under selection antibiotics as appropriate: HEKβ3/
451 α2δ1, Zeocin 300mg/ml (Invivogen) & Blasticidin 5mg/ml (Invivogen); HEKβ1b/α2δ1,
452 Puromycin 1mg/ml and Hygromycin-B 200mg/ml. Cell culture reagents were obtained from
453 Gibco/Invitrogen unless specified.

454 Selection antibiotics were removed before transfection and doxycycline 1µg/µl added in the
455 case of β3-expressing cells. Transient transfection was carried out using X-tremeGENE™ 9
456 reagent (Roche) following manufacturer's instructions. Total DNA was 1.5-1.6µg. For Western
457 blot experiments, human α1E-HA subunit and CDKL5 (HA-kinase domain or FLAG-full length)
458 were co-transfected in a 1:1 ratio, substituting kinase for empty pcdna3 vector in some cases.
459 For electrophysiological recordings α1E-HA, FLAG-CDKL5 full length and GFP (pcdna3) were
460 co-transfected at a ratio of 10:4:1 (HEK β3 cell line) or 8:4:1 (HEKβ1b cell line). To study
461 muscarinic regulation, human α1E-HA, FLAG-CDKL5, muscarinic receptor type 3/1
462 (CHRM3/1, Addgene) and GFP were co-expressed at a ratio of 8:4:3:1. For dopamine
463 modulation experiments, human α1E-HA, FLAG-CDKL5 and dopamine D2 receptor (gfp-
464 DRD2, Addgene) were co-transfected at a ratio of 2:0.75:1.

465 **Western Blotting**

466 Three different types of sample were used for Western blot experiments: 1) HEK293 cells 48
467 hr post-transfection, 2) Mouse brain tissue collected after cervical dislocation, followed by
468 dissection and snap-freezing in liquid nitrogen, 3) Human iPSC derived neurons obtained as

469 frozen pellets from Cleber Trujillo (UCSD, USA). Protocols for iPSC generation, patient *CDKL5*
470 mutations and related control details are described in [83]. All lysates were prepared in 1x/2x
471 sample buffer (Invitrogen) with 0.1-0.2 M dithiothreitol (Sigma). This was followed by
472 sonication, centrifugation at 13000g and denaturation at 70^0C, 10 min. Protein was loaded
473 onto NuPAGE 8% Bis-Tris polyacrylamide gels (Invitrogen) for electrophoresis and
474 subsequently transferred to polyvinylidene difluoride membranes (Millipore) for 15-22 hr at
475 20V in 10% MetOH, Tris Glycine buffer. Membranes were blocked for 30 min in 5-10%
476 skimmed milk and incubated with primary antibodies overnight at 4^0C or 1hr at room
477 temperature (RT). Secondary incubation in horseradish peroxidase-conjugated (HRP)
478 antibodies was for 1hr at RT. Chemiluminescence signals were detected using Amersham
479 ECL (Cytiva) and Amersham Imager (GE Healthcare). Analysis was perfomed using Fiji 2.1.
480 Phospho-S14/15 channel levels were measured as the ratio between pS14/15 Cav2.3 signal
481 and total Cav2.3 signal. Total channel levels are expressed as the ratio over loading control
482 GAPDH. Each replicate in a blot constitutes a data point normalized to the average internal
483 control signal in each blot. At least two independent immunoblot experiments with technical
484 replicates were used for quantification, as specified in figure legends.

485 Primary antibodies used in each sample were: mouse anti-HA 1:2000 (Biolegend, 901513;
486 HEK293), rabbit anti Cav2.3 N-terminus 1:250 (Covalab, custom 1, HEK293 & brain), rabbit
487 anti pS15 Cav2.3 1:500 (Covalab, custom 2, HEK293, brain & human neurons), mouse anti
488 Cav α1E 1:1000 (Synaptic Systems, 152411, human neurons), rabbit anti CDKL5 1:2000
489 (Atlas, HPA002847, HEK293), mouse anti GAPDH 1:50000 (Abcam, ab8245, brain & human
490 neurons). Custom made Cav2.3 Ser15 phosphospecific antibodies were raised by immunizing
491 rabbits with peptide PRPG(pS)GDGDSDQSRNC. Phosphorylated Cav2.3 antibody was
492 obtained after double purification. First, they were selected against non-phosphorylated
493 peptide PRPGSGDGDSDQSRNC. This antibody is used as total Cav2.3 antibody (custom 1).
494 Next the eluted fraction was purified again by binding to PRPG(pS)GDGDSDQSRNC -linked
495 beads, obtaining pSer15 Cav2.3 (custom 2). Secondary antibodies used were: donkey anti

496 rabbit HRP 1:10000 (Jackson, 711-035-152), donkey anti mouse HRP 1:10 000 (Jackson,
497 715-035-151).

498 ***In vitro* electrophysiology**

499 HEK293 cells

500 Cells were split 24hr after transfection and replated on glass coverslips and allowed to recover
501 overnight. Whole-cell patch clamp recordings in isolated cells were performed 48-72 hr post-
502 transfection at room temperature. Transfected cells were identified by GFP fluorescence. Data
503 were sampled at 20kHz and filtered at 1-2 kHz. Cells were continuously perfused (1ml/min)
504 with extracellular solution containing (in mM): NaCl 120, TEACl 20, HEPES 10, glucose 10,
505 KCl 5, $MgCl_2$ 1, $CaCl_2$ or $BaCl_2$ 5, pH 7.4 with NaOH. Pipettes (2.5-3.5 ΩM) were pulled from
506 borosilicate glass (1.2x0.69mm, Harvard Bioscience) and filled with the following intracellular
507 solutions adapted from [40] to minimize current run-down (in mM): CsMeS 140, EGTA 5, $MgCl_2$
508 0.5, MgATP 5, HEPES 10, for GPCR experiments; CsMethanesulfonate 125, TEACl 5, EGTA
509 5, MgATP 5, Na_3GTP 0.3, Na-phosphocreatine 5, Na-pyruvate 2.5, HEPES 10, pH 7.25, 285-
510 295 mOsm, all other recordings. Upon seal break, currents were evoked every 5/10s with a
511 step from -80/-100mV (holding potential, HP) to 0/+10mV. After an initial run-up period, steady
512 state current voltage (IV) relationships were obtained with 100ms depolarising test steps to
513 +60/+80 in 10mV increments every 10s. For voltage dependence of inactivation the protocol
514 consisted of a 1s pulse from -140 to +20mV in 10 mV increments, followed by a 50 ms test
515 pulse to 0 mV, every 10s. Peak currents (I_{peak}) in response to test voltages (V_{test}) were used
516 to plot IVs and measure the voltage dependence of activation and inactivation. Reversal
517 voltage (E_{rev}) was estimated by extrapolating a linear fit to the IV curve from +20-+40 mV.
518 Conductance (g) was calculated using the equation ($g=(I_{peak})/(V_{test}-E_{rev})$). Voltage of half-
519 maximal activation or inactivation ($V_{1/2}$) were measured by fitting with a Boltzmann equation
520 ($Y= A+(B-A)/(1+\exp((V-V_{1/2})/K))$ where Y is the conductance or the current, and A and B are
521 the minimum and maximum amplitudes of the fit. Time course of open state inactivation (τ_{inact})
522 was estimated by fitting a single exponential function to current decay in response to test

523 pulses. The average of 3 fits at each voltage was used. For all transfection conditions, cells
524 with outward currents >40% of the peak current at +10mV or with τ_{inact} that did not decay
525 uniformly with depolarization were excluded from analysis. Similarly, cells were not used for
526 current density or τ_{inact} comparisons if run-down was >30% of the maximal current recorded in
527 the experiment as this is known to affect inactivation time [40]. To examine recovery from
528 inactivation, an inactivating pulse to +10mV of 0.8-1s (pulse 1), was followed by a variable
529 recovery period (Δ150-200ms) and a test pulse to +10mV (pulse 2), at 0.1-0.3 Hz. Time course
530 of recovery was calculated using the ratio of I_{peak} in response to pulse 2/pulse 1 plotted against
531 duration of recovery period and fitted with single exponential equation. Carbachol, quinpirole
532 and PMA were bath applied at ~3 ml/min whilst activating Cav2.3 currents with brief monitoring
533 (25ms) test steps to 0 or +10mV, every 2, 5 or 10s, depending on speed of run-down. Upon
534 steady state, IVs were obtained. Cells included in the analysis showed no significant changes
535 in series resistance and a consistent shift in activation $V_{1/2}$, with current amplitude matching
536 between IV and brief monitoring steps. Leak and capacitance subtraction was applied to all
537 recordings using -P/5 protocol and series resistance compensated from 75-95% to keep
538 voltage error <5mV.

539 ***Ex vivo* electrophysiology**

540 Hippocampal slices

541 Mice older than P10 were anaesthetized by intraperitoneal injection of ketamine (80mg/kg)
542 and xylazine (10mg/kg). To avoid bias, the genotype was unknown at the time of experiment.
543 Animals were decapitated and the brain transferred to ice cold artificial cerebrospinal fluid
544 (standard aCSF) containing (in mM): NaCl 125, NaH_2PO_4 1.25, $NaHCO_3$ 26, KCl 2.5, glucose
545 25, $MgCl_2$ 1, $CaCl_2$ 1, saturated with carbogen. Cerebellum and olfactory bulb were discarded.
546 Coronal or transverse hippocampal slices (300µm) were prepared with a Leica VTS 1200S
547 vibratome and transferred to an immersion storage chamber containing bubbled aCSF at 35^0C
548 for 30 min. Slices were allowed to recover for a further 30 min at room temperature (RT) before
549 electrophysiology experiments. Somatic whole-cell patch clamp recordings were obtained

550 from CA1 pyramidal neurons using borosilicate electrodes (3-4.5 MΩ). Series resistance (R_s)
551 and input resistance (R_{in}) were monitored throughout recordings using a 100ms, -5mV step
552 from -60mV to evoke passive membrane responses. R_s was calculated from the amplitude of
553 the capacitive transient and R_{in} from the steady state currents. These were sampled at 20kHz
554 and filtered at 10kHz. The maximum change in Rs permitted was 25%.

555 *R-type Ca^{2+} currents* - Recordings were obtained from young neurons (P10-11) no longer than
556 6h post slicing using the blind technique. Currents were recorded at RT from P10-11 coronal
557 slices during bath application of a modified aCSF solution (in mM): NaCl 115, TEACl 10,
558 $NaHCO_3$ 26, KCl 2.5, NaH_2PO_4 1.25, glucose 25, $MgCl_2$ 1, $CaCl_2$ 2; and in presence of the
559 following inhibitors (in μM): TTX 0.5, gabazine 1, APV 25, NBQX 5, 4AP 5, Nifedipine 10
560 (Tocris), w-conotoxin GVIA 2, w-agatoxin IVA 0.2, w-conotoxin MVIIC 2 (Alomone) and BSA
561 1mg/ml. Drug stock solutions were prepared in water and stored at -20^{0}C. External solution
562 was constantly bubbled and re-circulated. Slices were exposed to ion channel inhibitors for at
563 least 20 min before voltage clamp acquisition. Patch pipettes were filled with (in mM):
564 CsMethanesulfonate 130, TEACl 10, Na-phosphocreatine 5, $MgATP_2$ 4, Na_3GTP 0.3, HEPES
565 10, EGTA 2 and biocytin 0.2% pH 7.3 with CsOH. After 10 min stabilization in the whole-cell
566 configuration, IV curves were obtained with voltage steps from -80 to +40, HP=-70mV. A -P/5
567 leak and capacitance subtraction protocol was used and R_s was compensated 65-85%, to
568 minimize voltage error. Capacitance (C_m) was calculated using equation: C_m [pF] = τ_m
569 [ms]/R_s[MΩ], where τ_m is the decay time constant of capacitative transients. Time course of
570 open state inactivation was estimated by iterative single exponential fit to current decay. A
571 positive correlation was found between τ_{inact} and C_m for C_m<80pF, thus this was established as
572 the cut off cell size criteria for inclusion in τ_{inact} comparisons. Cells with large cells outward
573 currents at depolarising voltages (>50% of the peak current at +10mV) were also excluded.

574 *Small-conductance Ca^{2+}-activated (SK) currents and excitatory postsynaptic currents (EPSC)-*
575 Recordings were obtained from adult neurons (5-6 weeks) in transverse slices. SK currents
576 were measured as tail currents following a 100ms step from -50 mV to +10mV (0.3 Hz) to

577 engage VGCCs. Standard aCSF ($CaCl_2$ 2mM, RT) was supplemented with (in μM): TTX 0.5,
578 TEA 1000 and XE991 5, to isolate SK currents by inhibiting temporally overlapping voltage-
579 gated Na^+ and K^+ conductances. The intracellular solution was (in mM): KGluconate 135, KCl
580 10, Na-phosphocreatine 10, $MgATP_2$ 2, Na_3GTP 0.3, HEPES 10, pH 7.3, supplemented with
581 8-cloro-phenylthio cAMP 50μM, to inhibit the slow afterhyperpolarizing current. SK current
582 identity was confirmed at the end of all experiments by reversible d-tubocurarine (dTC, 50μM)
583 inhibition. dTC-subtracted currents were used for quantification. Traces were sampled at 5
584 kHz and filtered at 1kHz. SK current amplitude was measured at the peak of the after-current
585 and charge as the integral 500ms post stimulus. EPSCs were isolated at -70 mV in standard
586 aCSF (1) ($CaCl_2$ 2.5mM, 30-32^{0}C) with gabazine 1 μM and Kgluconate-based internal solution.
587 Traces were sampled at 10kHz and filtered at 2kHz. Upon 5 min stabilization in whole-cell, a
588 2 min gap free trace was analysed using template-based event detection and threshold match
589 >3.

590 *Current clamp recordings* - Recordings were obtained from adult neurons (5-6 weeks) in
591 coronal slices in standard aCSF (2mM Ca^{2+}, 30-32^{0}C) and Kgluconate-based internal solution.
592 Membrane potential (V_{rest}) was measured throughout the recording with 0 current injection and
593 maintained around -65mV during stimulation. Input-output relationships were obtained with 1s
594 current injections from -100 to 450 pA in 50 pA increments. Traces were sampled at 10kHz
595 and filtered at 5kHz. Action potentials were identified with threshold-based event detection
596 (0mV) and amplitude measured from V_{rest}. Spike attenuation during the train was calculated
597 as ratio between last and first spike amplitudes. Depolarizing plateau potentials (DPPs) were
598 defined as sustained depolarizations >20mV upon stimulus termination. Medium duration
599 afterdepolarizations (ADPs) were measured 100ms post-1s step depolarization. Firing
600 patterns were compared using binomial tests or comparisons of non-linear least squares
601 regression fits to the data distribution. The effect of carbachol on the medium and slow
602 afterhyperpolarizations (mAHP and sAHP) was used as positive control for muscarinic
603 receptor activation. AHPs were evoked at -65mV by a burst of five 2nA, 2ms somatic current

604 injections at 100Hz every 20s and measured at the peak and 500ms post stimulus
605 respectively.

606 All patch clamp data was obtained with Multiclamp 700B, Digidata 1440A and pClamp™ 10
607 software (Molecular Devices). Data were analysed using Clampfit 10.7/11.2 and OriginPro
608 9.8. Liquid junction potential was not corrected.

609 ***In vivo* electrophysiology**

610 Chronic electrocorticogram recordings

611 Surgical procedures were performed in adult male and female mice (8-10 weeks old) using a
612 stereotaxic frame (Kopf) under isoflurane anaesthesia and temperature control. Each animal
613 was subcutaneously implanted with an electrocorticogram (ECoG) transmitter (A3022B-CC-
614 B45-B, Open Source Instruments, Inc.). The recording electrode was placed above the visual
615 cortex (AP -2, ML 1.5) and the ground electrode in the contralateral prefrontal hemisphere (AP
616 1.8, ML 1.5). Implanted WT and Hom S15A animals (total 18) were housed individually and
617 no drug treatment was given. The ECoG was recorded wirelessly (sampling frequency 512
618 Hz, band-pass filter 1-160 Hz) for two weeks using software from Open Source Instruments,
619 Inc. Simultaneous video recordings were obtained (6x/hour) using IP cameras from
620 Microseven (https://www.microseven.com/index.html). The coastline, kurtosis and power
621 spectrum analysis (1-160Hz) were performed using Python. Researchers were blinded to
622 animal genotype during data acquisition and analysis.

623 Kainic acid susceptibility

624 At the end of the chronic recordings, low dose 5mg/kg kainic acid (Tocris Bioscience)
625 dissolved in sterile saline was administrated intraperitoneally every 30 minutes to assess brain
626 susceptibility to increasing dosage of chemo convulsant. The clock started at the first injection
627 from 0 minute. Seizure severity was initially assessed while the experiment was ongoing at
628 10-minute intervals, using a modified Racine scale: 1. immobility; 2, hunched position with
629 facial jerks, 3. rearing and forelimb clonus, 4. persistent rearing and forelimb clonus, falling, 5.

630 generalized tonic clonic convulsions, or wild jumping [78]. These assessments were confirmed
631 by re-analyzing the video recordings. Latency measures the length of time from the start of
632 the experiment to the first indication of generalized seizure (Stage 5 on Racine scale). Both
633 kainic acid inductions and analysis were performed by a researcher blinded to the genotypes.
634 A total of 17 implanted mice were used for susceptibility experiments, one male mouse was
635 removed from the study due to surgical complications with the transmitter. In a subset of these
636 where transmitter performance was not compromised, ECoG recordings during seizure
637 inductions were recovered and used for quantification. Traces were analysed using semi-
638 automated seizure detection as described previously [77]. The cumulative coastline was
639 calculated from when the first epileptiform activity was detected until the mice reached
640 generalized seizure (stage 5).

641 **Behavioural analysis**

642 Home Cage monitoring

643 Two separate cohorts of WT and homozygous S15A Cav2.3 mice of both sexes and aged
644 between 12-16 weeks were used. Animals were housed individually and monitored using the
645 Digital Ventilated Cage system (DVC®,Techniplast, Italy). The DVC consists of standard size,
646 barcoded IVC units equipped with a 3x4 arrangement of cage-floor electrodes. Capacitance
647 sensing-based detection of animal position allows for real-time tracking of locomotion activity
648 24/7. Following a 2-week-acclimatization period, baseline activity was recorded and analysed.
649 Rotating wheels (Ø 4.4 in) were then introduced, and animals allowed to familiarize
650 themselves for another week before data collection. All activity metrics were calculated using
651 the DVC Analytics 3.4.0 platform [98]. For locomotion index, the average signal of all 12 cage
652 electrodes was used. Data were grouped in 60 min bins for each day.

653 Behaviour tests

654 Behaviour experiments were conducted in 8-week-old WT and homozygous S15A Cav2.3
655 littermates of both sexes, housed under an inverted light cycle. Mice were handled daily for

656 one week prior to experiments. All tests were video recorded for off-line analysis. Tracking
657 data were analysed using Ethovision XT 15 (Noldus Information Technology, Netherlands)
658 equipped with three-point (nose, body centre, and tail) detection settings. One cohort of mice
659 was used for all 7 tests, carried out in the order described below. Mice were allowed to
660 habituate to the testing room for at least an hour before the behaviour test.

661 Hind-Limb clasping – Mice were suspended by the middle of the tail and lifted 15 cm above
662 the ground; the extent of hind-limb clasping was recorded for 15 seconds. The room lighting
663 was kept at 90 Lux. Hind-limb clasping was scored from 0 to 3: score 0 = both hind limbs were
664 splayed outward away from the abdomen; score 1 = one hind limb retracted inward toward the
665 abdomen for at least 50% of the observation period; score 2 = both hind limbs partially
666 retracted inward toward the abdomen for at least 50% of the observation period; score 3 =
667 both hind limbs completely retracted inward toward the abdomen for at least 50% of the
668 observation period. Hind-limb extension reflex severity scores were calculated by averaging
669 three trials separated by 1 min.

670 Open field test - The apparatus consisted of an illuminated (70 lux) white floor PVC foam arena
671 (50 x 50 x 40 cm). A central zone (16 x 16 cm) was pre-defined. Test mice were placed in the
672 centre of the open field and allowed to explore the arena for 30 minutes. At the end of each
673 trial, the mouse was returned to the home cage and the arena was cleaned. Total distance
674 travelled in 30 minutes and percentage of time spent in the central zone were used as
675 measures of locomotor activity and anxiety levels, respectively.

676 Accelerating Rotarod test - Day 1: Mice walked on a rotating rod (Ugo Basile model 47650,
677 Italy) at constant speed (4 rpm) for three minutes for two acclimatization trials. Day 2: Each
678 mouse was placed on the rotating rod for three test trials, during which the rotation speed
679 gradually increased from 4 to 40 rpm within four minutes. The inter trial interval was 1 hr.
680 Performance was evaluated by measuring the latency to fall.

681 Three-chamber social interaction test – The apparatus consisted of a white rectangular PVC
682 foam arena (62x42x23 cm) divided into one central and two adjacent compartments of equal
683 size compartments connected by square openings. Empty cylindrical wire cages (Ø 8 cm,
684 height 18 cm) were placed in the lateral chambers. Each mouse was placed in the central
685 chamber and allowed to explore the arena for 10 min. The brightness of the room was kept at
686 10 lux. Chamber occupancy during habituation was equal between groups. After this, the
687 mouse was returned to the waiting cage for 3 minutes. To assess social preference, an
688 unfamiliar WT mouse of the same age, sex and strain (stranger 1) was gently introduced inside
689 one of the wire cages to serve as a social stimulus. An unfamiliar and inanimate object was
690 added to the other wire cage as the non-social stimulus. The test mouse was placed in the
691 apparatus containing the social and non-social stimuli for 10 minutes. After that, the test
692 mouse was removed and kept in the waiting cage for 3 minutes. All compartments were
693 cleaned with 30% ethanol solution before the next test phase. To assess preference for social
694 novelty, the non-social object from the previous test phase was replaced by an unfamiliar
695 mouse (stranger 2) and the previous stranger 1 (now familiar mouse) was placed into the wire
696 cage of the opposite compartment. The test mouse was placed in the central chamber and
697 allowed to explore the arena for the next 10 minutes, after which it was returned to the home
698 cage. The location of the novel and familiar mice with respect to the side compartments was
699 counterbalanced across trials. The exploration of the target mouse/object was scored when
700 the mouse's nose was detected within 2 cm from the cylindrical wire cage.

701 Y-maze spontaneous alternation test – Testing occurs in a Y-shaped maze with three arms
702 (1,2,3) made of opaque plastic (34 x 9 x 14 cm) oriented in a 120^0 angle. Each mouse was
703 randomly placed into one arm and allowed to explore the maze for 10 minutes. Room lighting
704 was kept at 10 lux. An arm entry was recorded manually when the mouse moved beyond the
705 central triangle of the maze and entered an arm with all four paws. Alternation behaviour was
706 defined as consecutive entries into each of the three arms in overlapping triplet sets (e.g.: 1,

707 2, 3 or 2, 1, 3 or 3, 2, 1). The percentage of alternations was calculated as the number of
708 actual alternations divided by the maximum possible number of arm entries.

709 Barnes-maze test – Twenty-four hours before training, the animal was habituated to the
710 apparatus and escape box for a minute. During the training phase (4 days), mice were trained
711 to locate the target hole (with an escape chamber underneath) from among 20 holes evenly
712 spaced around the perimeter of an elevated circular open field (Ø 96 cm). Each animal was
713 initially placed in the centre of the arena covered by an opaque cylinder, which was removed
714 10-20s after the start of the trial. Room lighting was kept at 635 lux. The mouse is then free to
715 explore the platform for 3 minutes using four visual cues to aid navigation. If the mouse does
716 not enter the escape chamber within 3 minutes the experimenter guides the mouse gently to
717 the escape box (20x11x7cm) and leaves the mouse inside for 1 min. This step is repeated two
718 more times a day (3 trials in total per day) with at least 20 minutes in between where the
719 mouse is placed back in its home cage. To assess learning, a probe test in carried out 24h
720 after the last training, where the escape box has been removed from the target hole. The
721 mouse is placed on the platform and free to explore it for 3 minutes. Distance to first: distance
722 walked from the centre of the arena to the target hole (centre-point detection); latency to first:
723 time to reach the target hole from the centre of the arena (centre-point detection); errors to
724 first are defined as checking any hole before reaching the escape box (nose-point detection).

725 Contextual fear conditioning – The fear conditioning chamber (27x27x35 cm, Ugo Basile, Italy)
726 was equipped with a shock grid floor and a digital Near Infrared Red Video Fear Conditioning
727 system. Mice from each genotype and sex were examined in four successive phases
728 comprising: conditioned acquisition (day 1), memory of the conditioned background context A
729 (day 2), exploration in new background context B (day 3) and memory extinction in the
730 conditioned context A (day 4-7).

731 Context A was characterized by a cubic shape, illuminated at 100 Lux and the presence of a
732 vanilla odour. The floor consisted of metal rods, mediating the foot shock. Context B was also
733 cubic shaped, not illuminated and without additional odour cues. On day 1: Mice were

734 introduced in the conditioning chambers scented with vanilla odour for 8 min and received 3
735 unconditioned stimuli (US: 1s, 0.25 mA foot shock, 2 min inter-trials interval). To examine the
736 conditioned response to the context, mice were reintroduced in the training context 24 h later
737 (day 2) and monitored for 5 minutes in the absence of the US. On day 3, the mice were
738 introduced to a new context (context B) for 5 min to examine whether freezing behaviour is
739 associated to a specific context (context A). During days 4-7 mice were placed back in context
740 A without US to assess extinction of the association of the specific context A and the US
741 (which is described as a form of new learning).

742 **Statistical Analysis**

743 Statistical analyses were performed in GraphPad Prism 9. Two-tailed Student's T tests and
744 one- or two-way ANOVA with Geisser-Greenhouse correction followed by Fisher's LSD test
745 were used for most statistical comparisons, unless otherwise specified. Repeated measures
746 ANOVA was used as appropriate if there were no missing values. Data are presented as mean
747 ± S.E.M. Box and whiskers (min to max) or violin plots are used to illustrate data spread and
748 frequency distribution respectively; percentile 25/75, median and mean are indicated by
749 lines/markers.

750 **Data availability**

751 The datasets generated and analysed during this study are available from the corresponding
752 authors on reasonable request.

753

754 **List of supplementary materials**

755 Supplementary Figures 1-4.

756

757

758

759 ## References

760 1. Guerrini R, Conti V, Mantegazza M, Balestrini S, Galanopoulou AS, Benfenati F.
761 Developmental and epileptic encephalopathies: from genetic heterogeneity to phenotypic
762 continuum. *Physiol Rev* **103**, 433-513 (2023).

763
764 2. Kalscheuer VM*, et al.* Disruption of the serine/threonine kinase 9 gene causes severe X-
765 linked infantile spasms and mental retardation. *American journal of human genetics* **72**,
766 1401-1411 (2003).

767
768 3. Olson HE*, et al.* Cyclin-Dependent Kinase-Like 5 Deficiency Disorder: Clinical Review. *Pediatr*
769 *Neurol* **97**, 18-25 (2019).

770
771 4. Van Bergen NJ*, et al.* CDKL5 deficiency disorder: molecular insights and mechanisms of
772 pathogenicity to fast-track therapeutic development. *Biochemical Society transactions* **50**,
773 1207-1224 (2022).

774
775 5. Leonard H, Downs J, Benke TA, Swanson L, Olson H, Demarest S. CDKL5 deficiency disorder:
776 clinical features, diagnosis, and management. *Lancet Neurol* **21**, 563-576 (2022).

777
778 6. Munoz IM*, et al.* Phosphoproteomic screening identifies physiological substrates of the
779 CDKL5 kinase. *The EMBO journal* **37**, (2018).

780
781 7. Hector RD*, et al.* CDKL5 variants: Improving our understanding of a rare neurologic disorder.
782 *Neurol Genet* **3**, e200 (2017).

783
784 8. Krishnaraj R, Ho G, Christodoulou J. RettBASE: Rett syndrome database update. *Human*
785 *mutation* **38**, 922-931 (2017).

786
787 9. Bahi-Buisson N*, et al.* Recurrent mutations in the CDKL5 gene: genotype-phenotype
788 relationships. *American journal of medical genetics Part A* **158A**, 1612-1619 (2012).

789
790 10. Symonds JD*, et al.* Incidence and phenotypes of childhood-onset genetic epilepsies: a
791 prospective population-based national cohort. *Brain : a journal of neurology* **142**, 2303-2318
792 (2019).

793
794 11. Lindy AS*, et al.* Diagnostic outcomes for genetic testing of 70 genes in 8565 patients with
795 epilepsy and neurodevelopmental disorders. *Epilepsia* **59**, 1062-1071 (2018).

796
797 12. Kothur K*, et al.* Diagnostic yield of targeted massively parallel sequencing in children with
798 epileptic encephalopathy. *Seizure* **59**, 132-140 (2018).

799
800 13. Bahi-Buisson N, Bienvenu T. CDKL5-Related Disorders: From Clinical Description to Molecular
801 Genetics. *Mol Syndromol* **2**, 137-152 (2012).

802
803 14. Siri B*, et al.* CDKL5 deficiency disorder in males: Five new variants and review of the
804 literature. *Eur J Paediatr Neurol* **33**, 9-20 (2021).

805
806 15. Wang IT*, et al.* Loss of CDKL5 disrupts kinome profile and event-related potentials leading to
807 autistic-like phenotypes in mice. *Proceedings of the National Academy of Sciences of the*
808 *United States of America* **109**, 21516-21521 (2012).

809
810 16. Hector RD*, et al.* Characterisation of CDKL5 Transcript Isoforms in Human and Mouse. *PloS*
811 *one* **11**, e0157758 (2016).

812
813 17. Hector RD, Dando O, Ritakari TE, Kind PC, Bailey ME, Cobb SR. Characterisation of Cdkl5
814 transcript isoforms in rat. *Gene* **603**, 21-26 (2017).

815
816 18. Okuda K*, et al.* CDKL5 controls postsynaptic localization of GluN2B-containing NMDA
817 receptors in the hippocampus and regulates seizure susceptibility. *Neurobiology of disease*
818 **106**, 158-170 (2017).

819
820 19. Rusconi L*, et al.* CDKL5 expression is modulated during neuronal development and its
821 subcellular distribution is tightly regulated by the C-terminal tail. *The Journal of biological*
822 *chemistry* **283**, 30101-30111 (2008).

823
824 20. Baltussen LL*, et al.* Chemical genetic identification of CDKL5 substrates reveals its role in
825 neuronal microtubule dynamics. *The EMBO journal* **37**, (2018).

826
827 21. Khanam T*, et al.* CDKL5 kinase controls transcription-coupled responses to DNA damage. *The*
828 *EMBO journal* **40**, e108271 (2021).

829
830 22. Kim JY*, et al.* A kinome-wide screen identifies a CDKL5-SOX9 regulatory axis in epithelial cell
831 death and kidney injury. *Nat Commun* **11**, 1924 (2020).

832
833 23. Zhou A, Han S, Zhou ZJ. Molecular and genetic insights into an infantile epileptic
834 encephalopathy - CDKL5 disorder. *Front Biol (Beijing)* **12**, 1-6 (2017).

835
836 24. Katayama S, Sueyoshi N, Inazu T, Kameshita I. Cyclin-Dependent Kinase-Like 5 (CDKL5):
837 Possible Cellular Signalling Targets and Involvement in CDKL5 Deficiency Disorder. *Neural*
838 *plasticity* **2020**, 6970190 (2020).

839
840 25. Gurgone A*, et al.* mGluR5 PAMs rescue cortical and behavioural defects in a mouse model of
841 CDKL5 deficiency disorder. *Neuropsychopharmacology*, (2022).

842
843 26. La Montanara P*, et al.* Cyclin-dependent-like kinase 5 is required for pain signaling in human
844 sensory neurons and mouse models. *Sci Transl Med* **12**, (2020).

845

27. Di Nardo A, Ruhmkorf A, Award P, Brennecke A, Fagiolini M, Sahin M. Phenotypic characterization of Cdkl5-knockdown neurons establishes elongated cilia as a functional assay for CDKL5 Deficiency Disorder. *Neuroscience research* **176**, 73-78 (2022).

28. Kontaxi C, Davenport EC, Kind PC, Cousin MA. Epilepsy-related CDKL5 deficiency slows synaptic vesicle endocytosis in central nerve terminals. *bioRxiv*, 2022.2003.2015.484308 (2022).

29. de Oliveira LS*, et al.* Enhanced hippocampal LTP but typical NMDA receptor and AMPA receptor function in a novel rat model of CDKL5 deficiency disorder. *bioRxiv*, 2022.2006.2029.497927 (2022).

30. Halpain S, Dehmelt L. The MAP1 family of microtubule-associated proteins. *Genome biology* **7**, 224 (2006).

31. Huang J, Zamponi GW. Regulation of voltage gated calcium channels by GPCRs and post-translational modification. *Curr Opin Pharmacol* **32**, 1-8 (2017).

32. Zamponi GW. Targeting voltage-gated calcium channels in neurological and psychiatric diseases. *Nature reviews Drug discovery* **15**, 19-34 (2016).

33. Dietrich D*, et al.* Functional specialization of presynaptic Cav2.3 Ca2+ channels. *Neuron* **39**, 483-496 (2003).

34. Parajuli LK*, et al.* Quantitative regional and ultrastructural localization of the Ca(v)2.3 subunit of R-type calcium channel in mouse brain. *J Neurosci* **32**, 13555-13567 (2012).

35. Sochivko D, Pereverzev A, Smyth N, Gissel C, Schneider T, Beck H. The Ca(V)2.3 Ca(2+) channel subunit contributes to R-type Ca(2+) currents in murine hippocampal and neocortical neurones. *The Journal of physiology* **542**, 699-710 (2002).

36. Zhang JF*, et al.* Distinctive pharmacology and kinetics of cloned neuronal Ca2+ channels and their possible counterparts in mammalian CNS neurons. *Neuropharmacology* **32**, 1075-1088 (1993).

37. Lee SC, Choi S, Lee T, Kim HL, Chin H, Shin HS. Molecular basis of R-type calcium channels in central amygdala neurons of the mouse. *Proceedings of the National Academy of Sciences of the United States of America* **99**, 3276-3281 (2002).

38. Schneider T*, et al.* Molecular analysis and functional expression of the human type E neuronal Ca2+ channel alpha 1 subunit. *Recept Channels* **2**, 255-270 (1994).

888 39. Soong TW, Stea A, Hodson CD, Dubel SJ, Vincent SR, Snutch TP. Structure and functional
889 expression of a member of the low voltage-activated calcium channel family. *Science* **260**,
890 1133-1136 (1993).

891
892 40. Neumaier F, Alpdogan S, Hescheler J, Schneider T. Protein phosphorylation maintains the
893 normal function of cloned human Cav2.3 channels. *J Gen Physiol* **150**, 491-510 (2018).

894
895 41. Schneider T, Alpdogan S, Hescheler J, Neumaier F. In vitro and in vivo phosphorylation of the
896 Cav2.3 voltage-gated R-type calcium channel. *Channels (Austin)* **12**, 326-334 (2018).

897
898 42. Proft J, Weiss N. G protein regulation of neuronal calcium channels: back to the future. *Mol*
899 *Pharmacol* **87**, 890-906 (2015).

900
901 43. Helbig KL*, et al.* De Novo Pathogenic Variants in CACNA1E Cause Developmental and
902 Epileptic Encephalopathy with Contractures, Macrocephaly, and Dyskinesias. *American*
903 *journal of human genetics* **103**, 666-678 (2018).

904
905 44. Heyne HO*, et al.* De novo variants in neurodevelopmental disorders with epilepsy. *Nature*
906 *genetics* **50**, 1048-1053 (2018).

907
908 45. Happ HC, Carvill GL. A 2020 View on the Genetics of Developmental and Epileptic
909 Encephalopathies. *Epilepsy Curr* **20**, 90-96 (2020).

910
911 46. Steward CA*, et al.* Re-annotation of 191 developmental and epileptic encephalopathy-
912 associated genes unmasks de novo variants in SCN1A. *NPJ Genom Med* **4**, 31 (2019).

913
914 47. Mann M. Functional and quantitative proteomics using SILAC. *Nature reviews Molecular cell*
915 *biology* **7**, 952-958 (2006).

916
917 48. Amendola E*, et al.* Mapping pathological phenotypes in a mouse model of CDKL5 disorder.
918 *PloS one* **9**, e91613 (2014).

919
920 49. Weiergraber M*, et al.* Altered seizure susceptibility in mice lacking the Ca(v)2.3 E-type Ca2+
921 channel. *Epilepsia* **47**, 839-850 (2006).

922
923 50. Weiergraber M, Kamp MA, Radhakrishnan K, Hescheler J, Schneider T. The Ca(v)2.3 voltage-
924 gated calcium channel in epileptogenesis--shedding new light on an enigmatic channel.
925 *Neurosci Biobehav Rev* **30**, 1122-1144 (2006).

926
927 51. Weiergraber M, Henry M, Radhakrishnan K, Hescheler J, Schneider T. Hippocampal seizure
928 resistance and reduced neuronal excitotoxicity in mice lacking the Cav2.3 E/R-type voltage-
929 gated calcium channel. *Journal of neurophysiology* **97**, 3660-3669 (2007).

930

931 52. Jones LP, Wei SK, Yue DT. Mechanism of auxiliary subunit modulation of neuronal alpha1E
932 calcium channels. *J Gen Physiol* **112**, 125-143 (1998).

933
934 53. Buraei Z, Yang J. The ss subunit of voltage-gated Ca2+ channels. *Physiol Rev* **90**, 1461-1506
935 (2010).

936
937 54. Muller CS*, et al.* Quantitative proteomics of the Cav2 channel nano-environments in the
938 mammalian brain. *Proceedings of the National Academy of Sciences of the United States of*
939 *America* **107**, 14950-14957 (2010).

940
941 55. Tai C, Kuzmiski JB, MacVicar BA. Muscarinic enhancement of R-type calcium currents in
942 hippocampal CA1 pyramidal neurons. *J Neurosci* **26**, 6249-6258 (2006).

943
944 56. Bannister RA, Melliti K, Adams BA. Differential modulation of CaV2.3 Ca2+ channels by
945 Galphaq/11-coupled muscarinic receptors. *Mol Pharmacol* **65**, 381-388 (2004).

946
947 57. Meza U, Bannister R, Melliti K, Adams B. Biphasic, opposing modulation of cloned neuronal
948 alpha1E Ca channels by distinct signaling pathways coupled to M2 muscarinic acetylcholine
949 receptors. *J Neurosci* **19**, 6806-6817 (1999).

950
951 58. Fraser DD, MacVicar BA. Cholinergic-dependent plateau potential in hippocampal CA1
952 pyramidal neurons. *J Neurosci* **16**, 4113-4128 (1996).

953
954 59. Page KM, Canti C, Stephens GJ, Berrow NS, Dolphin AC. Identification of the amino terminus
955 of neuronal Ca2+ channel alpha1 subunits alpha1B and alpha1E as an essential determinant
956 of G-protein modulation. *J Neurosci* **18**, 4815-4824 (1998).

957
958 60. Canti C, Page KM, Stephens GJ, Dolphin AC. Identification of residues in the N terminus of
959 alpha1B critical for inhibition of the voltage-dependent calcium channel by Gbeta gamma. *J*
960 *Neurosci* **19**, 6855-6864 (1999).

961
962 61. Fang H*, et al.* Role of alpha1 2.3 subunit I-II linker sites in the enhancement of Ca(v) 2.3
963 current by phorbol 12-myristate 13-acetate and acetyl-beta-methylcholine. *The Journal of*
964 *biological chemistry* **280**, 23559-23565 (2005).

965
966 62. Buchanan KA, Petrovic MM, Chamberlain SE, Marrion NV, Mellor JR. Facilitation of long-term
967 potentiation by muscarinic M(1) receptors is mediated by inhibition of SK channels. *Neuron*
968 **68**, 948-963 (2010).

969
970 63. Park JY, Spruston N. Synergistic actions of metabotropic acetylcholine and glutamate
971 receptors on the excitability of hippocampal CA1 pyramidal neurons. *J Neurosci* **32**, 6081-
972 6091 (2012).

973

64. Kawasaki H, Palmieri C, Avoli M. Muscarinic receptor activation induces depolarizing plateau potentials in bursting neurons of the rat subiculum. *Journal of neurophysiology* **82**, 2590-2601 (1999).

65. Williams SR, Fletcher LN. A Dendritic Substrate for the Cholinergic Control of Neocortical Output Neurons. *Neuron* **101**, 486-499 e484 (2019).

66. Park JY*, et al.* A post-burst after depolarization is mediated by group i metabotropic glutamate receptor-dependent upregulation of Ca(v)2.3 R-type calcium channels in CA1 pyramidal neurons. *PLoS biology* **8**, e1000534 (2010).

67. Kuzmiski JB, Barr W, Zamponi GW, MacVicar BA. Topiramate inhibits the initiation of plateau potentials in CA1 neurons by depressing R-type calcium channels. *Epilepsia* **46**, 481-489 (2005).

68. Brown DA, Passmore GM. Neural KCNQ (Kv7) channels. *Br J Pharmacol* **156**, 1185-1195 (2009).

69. Stocker M, Hirzel K, D'Hoedt D, Pedarzani P. Matching molecules to function: neuronal Ca2+-activated K+ channels and afterhyperpolarizations. *Toxicon* **43**, 933-949 (2004).

70. Bloodgood BL, Sabatini BL. Nonlinear regulation of unitary synaptic signals by CaV(2.3) voltage-sensitive calcium channels located in dendritic spines. *Neuron* **53**, 249-260 (2007).

71. Murphy JG*, et al.* R-type voltage-gated Ca(2+) channels mediate A-type K(+) current regulation of synaptic input in hippocampal dendrites. *Cell Rep* **38**, 110264 (2022).

72. Terzic B*, et al.* Temporal manipulation of Cdkl5 reveals essential postdevelopmental functions and reversible CDKL5 deficiency disorder-related deficits. *J Clin Invest* **131**, (2021).

73. Okuda K, Takao K, Watanabe A, Miyakawa T, Mizuguchi M, Tanaka T. Comprehensive behavioral analysis of the Cdkl5 knockout mice revealed significant enhancement in anxiety- and fear-related behaviors and impairment in both acquisition and long-term retention of spatial reference memory. *PloS one* **13**, e0196587 (2018).

74. Adhikari A*, et al.* Touchscreen cognitive deficits, hyperexcitability and hyperactivity in males and females using two models of Cdkl5 deficiency. *Human molecular genetics* **31**, 3032-3050 (2022).

75. Terzic B*, et al.* X-linked cellular mosaicism underlies age-dependent occurrence of seizure-like events in mouse models of CDKL5 deficiency disorder. *Neurobiology of disease* **148**, 105176 (2021).

1017 76. Wang HT*, et al.* CDKL5 deficiency in forebrain glutamatergic neurons results in recurrent
1018 spontaneous seizures. *Epilepsia* **62**, 517-528 (2021).

1019
1020 77. Colasante G*, et al.* In vivo CRISPRa decreases seizures and rescues cognitive deficits in a
1021 rodent model of epilepsy. *Brain : a journal of neurology* **143**, 891-905 (2020).

1022
1023 78. Tse K, Puttachary S, Beamer E, Sills GJ, Thippeswamy T. Advantages of repeated low dose
1024 against single high dose of kainate in C57BL/6J mouse model of status epilepticus:
1025 behavioral and electroencephalographic studies. *PloS one* **9**, e96622 (2014).

1026
1027 79. Page KM*, et al.* N terminus is key to the dominant negative suppression of Ca(V)2 calcium
1028 channels: implications for episodic ataxia type 2. *The Journal of biological chemistry* **285**,
1029 835-844 (2010).

1030
1031 80. Stephens GJ, Page KM, Bogdanov Y, Dolphin AC. The alpha1B Ca2+ channel amino terminus
1032 contributes determinants for beta subunit-mediated voltage-dependent inactivation
1033 properties. *The Journal of physiology* **525 Pt 2**, 377-390 (2000).

1034
1035 81. Williams ME*, et al.* Structure and functional characterization of neuronal alpha 1E calcium
1036 channel subtypes. *The Journal of biological chemistry* **269**, 22347-22357 (1994).

1037
1038 82. Artoni P*, et al.* Deep learning of spontaneous arousal fluctuations detects early cholinergic
1039 defects across neurodevelopmental mouse models and patients. *Proceedings of the National*
1040 *Academy of Sciences of the United States of America* **117**, 23298-23303 (2020).

1041
1042 83. Negraes PD*, et al.* Altered network and rescue of human neurons derived from individuals
1043 with early-onset genetic epilepsy. *Molecular psychiatry* **26**, 7047-7068 (2021).

1044
1045 84. Yennawar M, White RS, Jensen FE. AMPA Receptor Dysregulation and Therapeutic
1046 Interventions in a Mouse Model of CDKL5 Deficiency Disorder. *J Neurosci* **39**, 4814-4828
1047 (2019).

1048
1049 85. Tang S*, et al.* Loss of CDKL5 in Glutamatergic Neurons Disrupts Hippocampal Microcircuitry
1050 and Leads to Memory Impairment in Mice. *J Neurosci* **37**, 7420-7437 (2017).

1051
1052 86. Kamaludin AA*, et al.* Muscle dysfunction caused by loss of Magel2 in a mouse model of
1053 Prader-Willi and Schaaf-Yang syndromes. *Human molecular genetics* **25**, 3798-3809 (2016).

1054
1055 87. Ruiz A*, et al.* Improvement of muscle strength in a mouse model for congenital myopathy
1056 treated with HDAC and DNA methyltransferase inhibitors. *eLife* **11**, (2022).

1057
1058 88. Tang S*, et al.* Altered NMDAR signaling underlies autistic-like features in mouse models of
1059 CDKL5 deficiency disorder. *Nat Commun* **10**, 2655 (2019).

1060

1061 89. Weiergraber M, Henry M, Ho MS, Struck H, Hescheler J, Schneider T. Altered thalamocortical
1062 rhythmicity in Ca(v)2.3-deficient mice. *Molecular and cellular neurosciences* **39**, 605-618
1063 (2008).

1064
1065 90. Zaman T*, et al.* Cav2.3 channels are critical for oscillatory burst discharges in the reticular
1066 thalamus and absence epilepsy. *Neuron* **70**, 95-108 (2011).

1067
1068 91. Wormuth C*, et al.* Review: Cav2.3 R-type Voltage-Gated Ca(2+) Channels - Functional
1069 Implications in Convulsive and Non-convulsive Seizure Activity. *Open Neurol J* **10**, 99-126
1070 (2016).

1071
1072 92. Gao Y*, et al.* Gene replacement ameliorates deficits in mouse and human models of cyclin-
1073 dependent kinase-like 5 disorder. *Brain : a journal of neurology* **143**, 811-832 (2020).

1074
1075 93. Gray EE*, et al.* Disruption of GpI mGluR-Dependent Cav2.3 Translation in a Mouse Model of
1076 Fragile X Syndrome. *J Neurosci* **39**, 7453-7464 (2019).

1077
1078 94. Suzuki T*, et al.* Mutations in EFHC1 cause juvenile myoclonic epilepsy. *Nature genetics* **36**,
1079 842-849 (2004).

1080
1081 95. Benkert J*, et al.* Cav2.3 channels contribute to dopaminergic neuron loss in a model of
1082 Parkinson's disease. *Nat Commun* **10**, 5094 (2019).

1083
1084 96. Siller A*, et al.* beta2-subunit alternative splicing stabilizes Cav2.3 Ca(2+) channel activity
1085 during continuous midbrain dopamine neuron-like activity. *eLife* **11**, (2022).

1086
1087 97. Shakeri B, Bourdin B, Demers-Giroux PO, Sauve R, Parent L. A quartet of leucine residues in
1088 the guanylate kinase domain of CaVbeta determines the plasma membrane density of the
1089 CaV2.3 channel. *The Journal of biological chemistry* **287**, 32835-32847 (2012).

1090
1091 98. Iannello F. Non-intrusive high throughput automated data collection from the home cage.
1092 *Heliyon* **5**, e01454 (2019).

1093

1094

1095

1096

1097

1098

1099

Acknowledgements

We thank Ultanir lab members for valuable discussion and thoughtful comments. We thank Helen Flynn for valuable assistance with mass spectrometry. We thank Crick GEMS team for creation of CACNA1E S15A mice. This work was supported by the Francis Crick Institute which receives its core funding from Cancer Research UK (CC2037), the UK Medical Research Council (CC2037), and the Wellcome Trust (CC2037); Loulou Foundation Project Grant (11015); Crick-MSD Framework collaboration grant (11202). For the purpose of Open Access, the author has applied a CC BY public copyright licence to any Author Accepted Manuscript version arising from this submission.

Author contributions

M.S.C., L.L.B., G.L. and S.K.U. designed the experiments. M.S.C. performed and analysed electrophysiology and biochemistry experiments. L.L.B. performed mass spectrometry. Y.Q. and G.L. conducted/ analysed EEG and kainic acid-induced seizure experiments. A.T.L. and M.S.C. performed behaviour experiments/ analysis. L.S., S.M., S.C. provided technical assistance in molecular biology and electrophysiology. M.S.C. and S.K.U. wrote the initial version of the manuscript. J.R. contributed to the original draft and review/editing along with all authors.

Competing interests

The authors declare no competing interest.

Materials and Correspondence

Correspondence and material requests should be addressed to Sila K. Ultanir and Marisol Sampedro-Castañeda

Figure 1

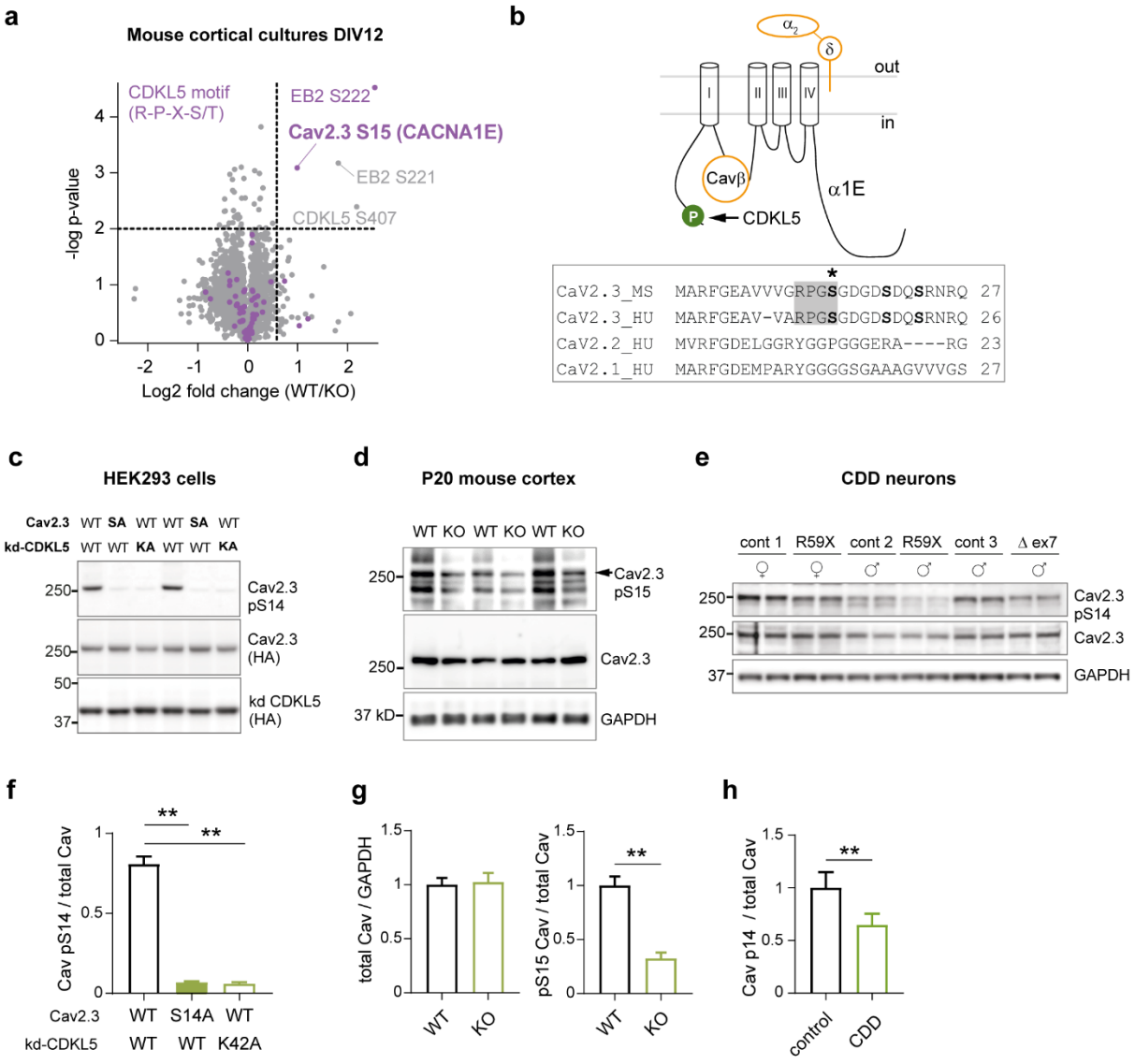

1129

1130 **Fig. 1: Identification and validation of Cav2.3 as substrate of CDKL5 kinase. a** Volcano
1131 plot of differential phosphoprotein levels between WT and CDKL5 KO primary neurons,
1132 obtained using SILAC based quantitative proteomics (5 embryos/genotype). Each point
1133 represents one peptide; those with CDKL5 consensus motif RPXS/T are highlighted in
1134 magenta. The x axis shows log2 transformed fold change in phosphopeptide levels between
1135 genotypes and the y axis shows significance as -log10 transformed p value. Significance was
1136 established as indicated by the dotted lines (p<0.01, fold change 1.5, one sample t test). **b**
1137 Top: Schematic depiction of Cav2.3 formed of α1E channel pore subunit and associated

1138 proteins Cavβ and α2δ. CDKL5 phosphorylation site at α1E S15/14 is highlighted in green.
1139 Bottom: Alignment of proximal N-terminus of mouse and human Cav2.3 and related human
1140 Cav2.1 and 2.2 channel proteins. *S is the site of CDKL5 phosphorylation. **c** Western blot of
1141 HEK293 cells stably expressing human β3/α2δ1 subunits and transiently co-transfected with
1142 human HA-α1E (Cav2.3: WT or S14A mutant) and HA-CDKL5 kinase domain (kd CDKL5: WT
1143 or K42A mutant). S14 phosphorylation (pS14 Cav2.3) was detected with a custom made
1144 phosphoantibody. **d** Western blot of P20 cortices from WT and CDKL5 KO mice. **e** Western
1145 blot of iPSC-derived forebrain neurons from three CDD patients and related controls (parents)
1146 at 6 weeks of differentiation. Gender and *CDKL5* mutation are specified [83]. **f** Quantification for
1147 immunoblot in **c** (**p<0.0001 Kruskal-Wallis ANOVA & Dunn's test, n=11, 4 blots, 2
1148 transfections). **g** Quantification for immunoblot in **d** (**p<0.0001 two tailed unpaired t test, n=9,
1149 3 blots, 6 mice/genotype). **h** Quantification for WB in **e** (**p<0.005 two tailed paired t test, n=6,
1150 2 blots, 2 technical replicates). For antibodies used see Methods.

Figure 2

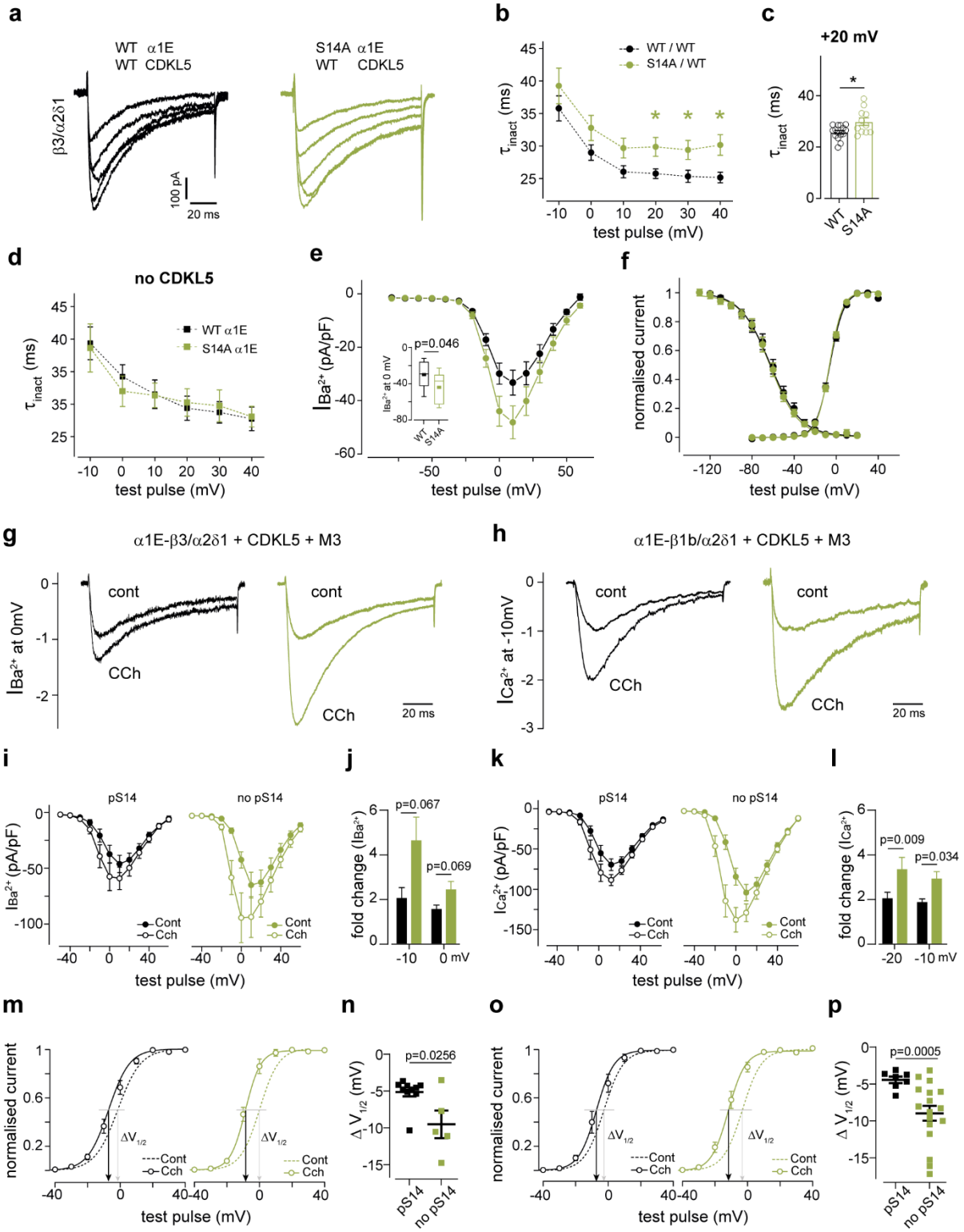

Fig. 2: Functional characterization of phospho-Ser14 Cav2.3 in HEK 293 cells. a Depolarization-evoked current responses in HEK293 cells stably expressing human β3/α2δ1

1154 subunits and co-transfected with human Cav2.3 (WT α1E or S14A α1E) and FLAG-CDKL5
1155 full length (WT CDKL5). Colours denote different construct combinations. Traces show steps
1156 from -10 to +30mV from -80mV; Ba^{2+} was charge carrier **b** Open channel inactivation tau
1157 (τ_{inact}) for Cav2.3 with (WT/WT, n=13-15) and without (S14A/WT, n=11-13) CDKL5
1158 phosphorylation (*p=0.02, 0.03 & 0.01 at +10, +20 & +40 mV Two-Way ANOVA, Fisher's
1159 LSD). Data were acquired using 100ms voltage steps from -80mV in +10mV increments every
1160 10s. **c** Individual data points for τ_{inact} at +20mV (*p=0.01, two-tailed unpaired t test). **d** WT or
1161 phophomutant S14A Cav2.3 inactivation in the same cell line in absence of CDKL5 (n=7-9;
1162 p>0.05 Two-Way ANOVA); Ca^{2+} was charge carrier. **e** Current voltage relationship for cells in
1163 **b**. Inset: comparison of current density at 0mV (inset, two-tailed unpaired t test). **f** Normalised
1164 Cav2.3 current conductance and voltage dependence of inactivation for the same transfection
1165 conditions. Activation $V_{1/2,}$ n: WT/WT -6±1 mV, 15; S14A/WT -6±1 mV,12; Inactivation $V_{1/2}$, n:
1166 WT/WT -61±3 mV,10; S14A/WT -62±2 mV,11 (p>0.05, two tailed unpaired t tests). For
1167 inactivation protocol see Methods. Solid lines are Boltzman fits to the average data points **g**
1168 Normalised Ba^{2+} currents in the β3/α2δ1-cell line or **h** Ca^{2+} currents in the β1/α2δ1-cell line,
1169 co-transfected with α1E (WT or S14A), WT CDKL5 and muscarinic type 3 receptor (M3), in
1170 presence and absence of carbachol (CCh) 30 and 10 μM, respectively. HP= -100mV. **i** IV
1171 curves and **j** CCh-induced change in current amplitude for experiment in **g** (pS14 n=8, no
1172 pS14 n=7, Two-Way ANOVA, Fisher's LSD). **k** IV curves and **l** CCh-induced change in current
1173 amplitude for experiment in **h** (pS14 n=7, no pS14 n=16, TW ANOVA, Fisher's LSD). **m**
1174 Conductance plots for experiment in **g** and **n** Corresponding change in activation ($V_{1/2}$: -5±0.6
1175 *vs*. -10±1.9 mV, Kolmogorov-Smirnov). **o** Conductance plots for experiment in **h** and **p**
1176 corresponding change in activation ($V_{1/2}$: -4±0.5 *vs* -9±1 mV, Welch's t test). From **l-p**, 'pS14'
1177 refers to WT α1E/WT CDKL5; 'no pS14' refers to S14A α1E /WT CDKL5 and α1E WT /K42R*
1178 CDKL5 conditions pulled together.

Figure 3

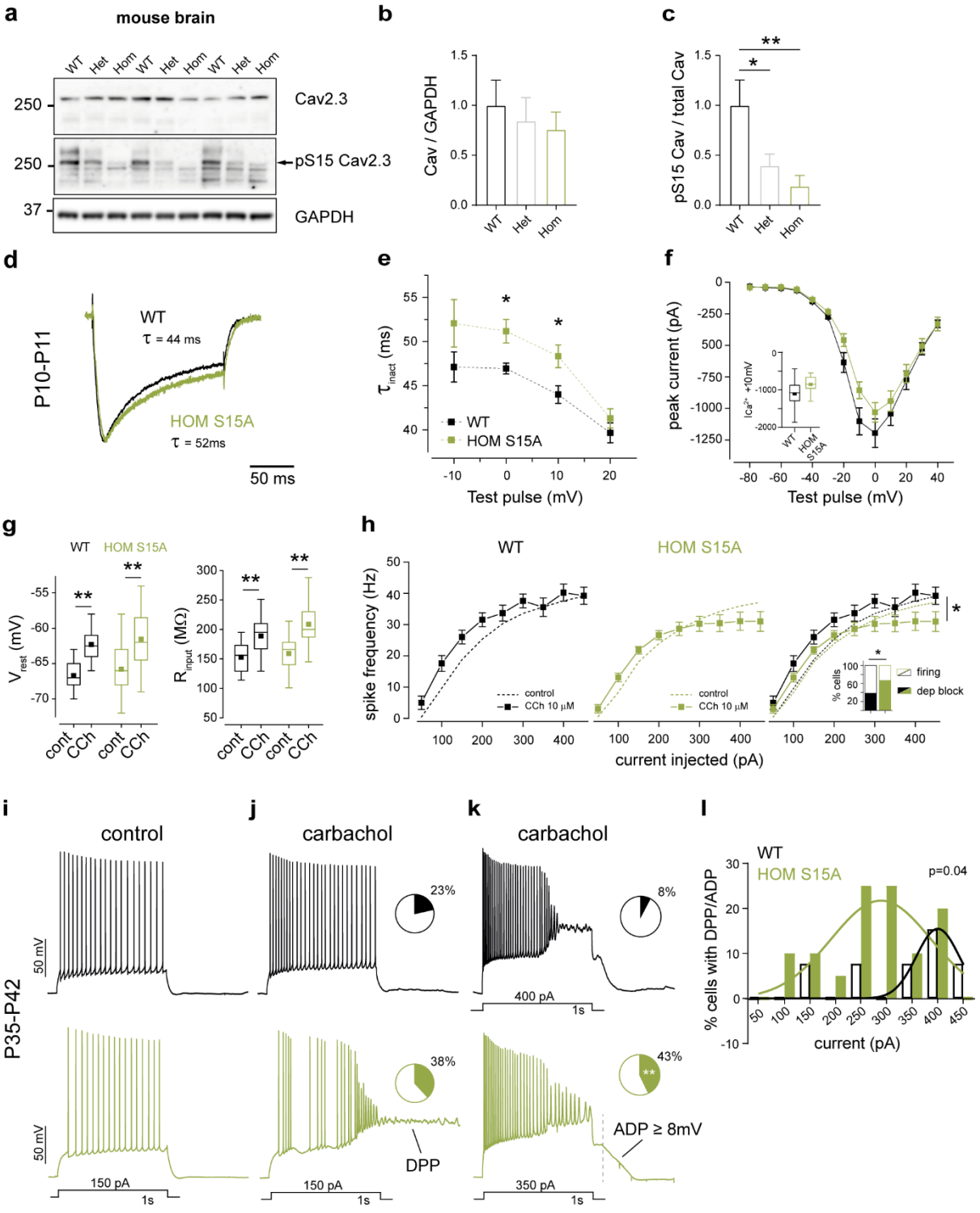

1179

1180 **Fig. 3: Physiological properties and cholinergic neuromodulation of hippocampal CA1**

1181 **neurons from WT and phosphomutant mice. a** WB validation of CRISPR-generated Cav2.3

1182 Ser15Ala mutant mice using a pS15 phosphoantibody in whole-brain lysates from 12-week-

1183 old WT, Heterozygous S15A and Homozygous S15A mice. **b** Quantification of total Cav2.3
1184 (p>0.05 One-Way ANOVA) and **c** relative phospho-S15 Cav2.3 (*p=0.029, **0.006 One-Way
1185 ANOVA, Fisher's LSD) expression (n=5, 2 blots, 3 mice/genotype). **d** Normalised R-type Ca^{2+}
1186 current in neurons from young mice of each genotype during a step from -60 to 0 mV in
1187 presence of Na^{+}, K^{+}, Ca^{2+} and synaptic channel inhibitors. **e** R-type current inactivation tau
1188 (τ_{inact}) at maximal activation voltages (*p=0.01 Two-Way Repeated Measures ANOVA,
1189 Fisher's LSD) and **f** average IV curve for all P10-11cells recorded (p>0.05), (n=13 neurons, 4-
1190 5 mice/genotype). Data for -10mV step is shown in the inset (p=0.06, two-tailed unpaired t
1191 test). **g** Membrane resting potential (V_{rest}, left) and input resistance (R_{input}, right) of adult
1192 neurons (WT n=13, HOM S15A n=17; 7 mice/genotype) in control conditions and after 10μM
1193 carbachol (CCh) application (**p<0.002, two-tailed paired t test). **h** Input/output curves for the
1194 same neurons (WT n=9, HOM n=13, *p<0.028 Two-Way Repeated Measures ANOVA) and
1195 percentage of cells with CCh-induced depolarization block (inset, WT n=13, HOM n=21,
1196 *p<0.012, binomial test). **i** Representative control action potential trains evoked in WT (top)
1197 and HOM S15A (bottom) CA1 cells by 1s-long current injections. Membrane was held at -
1198 65mV. **j** Same cells as **i** upon application of CCh and representative depolarising plateau
1199 potential (DPP), observed at some current injections in both genotypes; insets: fraction of cells
1200 with at least one DPP in each genotype group (WT n=13, HOM n=21, p>0.05 binomial test).
1201 **k** Same cells as **j** at higher stimulation illustrating sustained depolarization and AP block (top)
1202 or attenuation (bottom) towards the end of the stimulus and long-lasting large amplitude
1203 afterdepolarizations (ADP). Like DPPs, these ADPs were present at some current injections
1204 in a fraction of cells in both groups of mice (inset, WT n=13, HOM n=21, **p<0.004, binomial
1205 test). **l** Percentage of cells displaying sustained DPPs or ADPs upon stimulus termination at
1206 each current injection step (non-linear fit comparison).

Figure 4

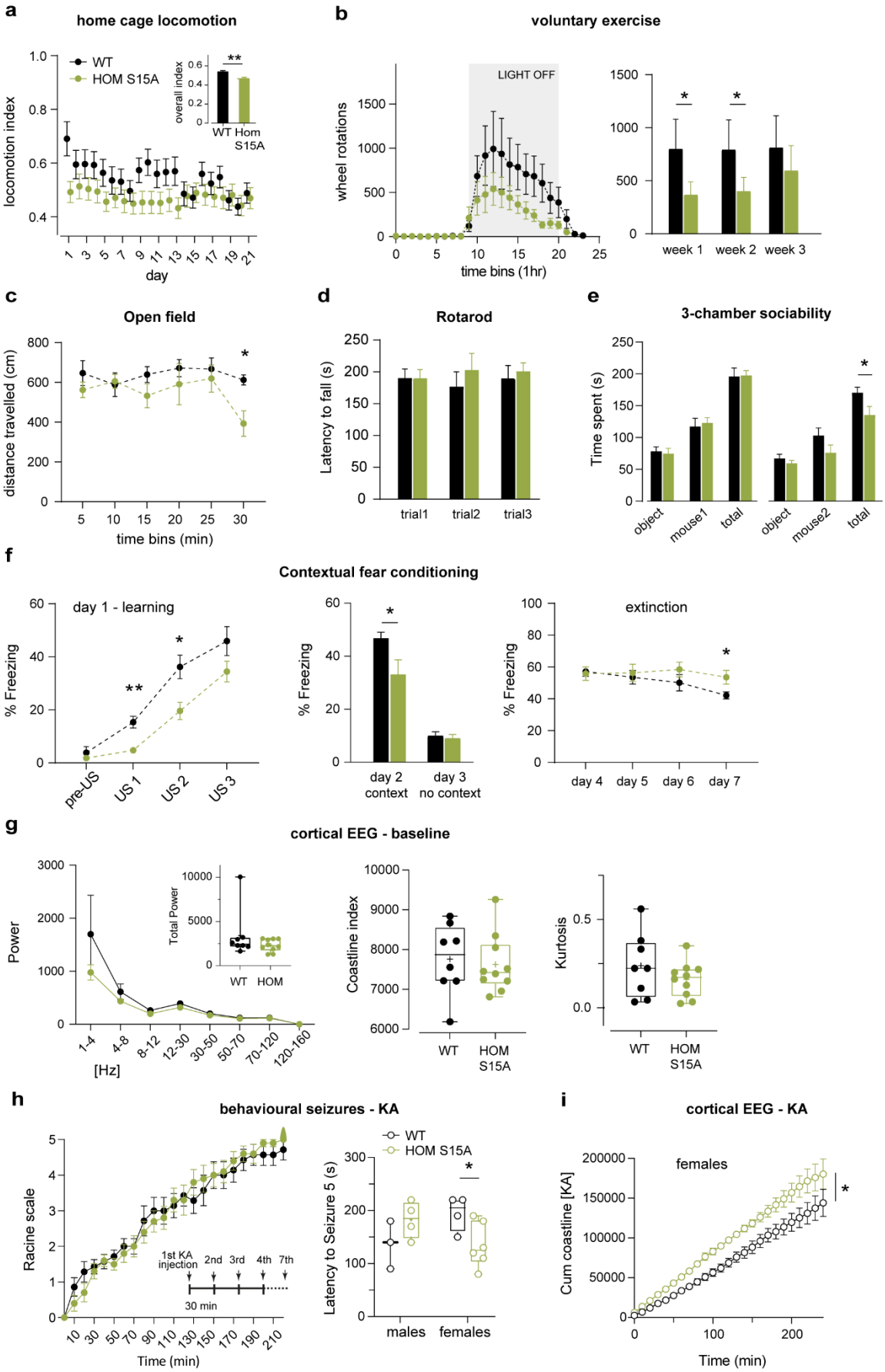

1207

1208 **Fig. 4: *In vivo* phenotypic characterization of Cav2.3 S15A mice**. **a** Average home cage
1209 night-time locomotion of WT and HOM S15A mice (N=9) per day and overall locomotion index
1210 (inset) in a three-week period (**p<0.0001, Welch's t test). **b** left: wheel rotations per hour
1211 during voluntary exercise activity for the same mouse cohort as **a**, over a two-week period;
1212 right: overall dark cycle average rotations in each group for three consecutive weeks (week 1
1213 *p=0.017, week 2 *p=0.049 Two-Way ANOVA, Fisher's LSD). **c** Total distance travelled by
1214 WT (N=8) and HOM S15A (n=7) mice in an open field arena (p<0.013 at 30 min Two-Way
1215 ANOVA, Fisher's LSD). **d** Accelerating rotarod performance for the same cohort as **c** (p>0.05,
1216 TW ANOVA). Animal weights were equal (WT=25±4 g, HOM=25±5 g, p>0.05, two-tailed
1217 unpaired t test). **e** Social, non-social and total exploration times during a 10min three-chamber
1218 sociability test (*p=0.04, two-tailed unpaired t test). In habituation trials, chamber occupancy
1219 was equal between groups. **f** Freezing behaviour during learning day 1 (left, *p=0.01,
1220 **p=0.002), associative memory test day 2+3 (middle, *p=0.03) and memory extinction test
1221 days 4-7 (right, *p=0.043), in a fear-conditioning experiment with tactile and olfactory cues
1222 (Two-tailed unpaired t test or Two-Way Repeated Measures ANOVA, Fisher's LSD). **g** left:
1223 two-week baseline ECoG spectral analysis and total power (inset) in WT (N=8) and HOMS15A
1224 (N=10) 9-12 week-old mice; corresponding coastline index (middle) and kurtosis (right)
1225 (p>0.05, Two-Way ANOVA and two-tailed unpaired t tests). No sex differences were
1226 observed. **h** left: behavioural scoring of kainic acid (KA)-induced seizures (WT N=7,
1227 HOMS15A N=10, p>0.05, Two-Way ANOVA) using repetitive 5mg/kg i.p. injections (inset);
1228 right: latency to stage 5 tonic clonic seizures per gender (males, p>0.05; females *p<0.0449,
1229 two-tailed unpaired t test). **i** Corresponding cumulative ECoG coastline during KA seizures in
1230 females (WT N=3, HOM S15A N=4, *p<0.018, Two-Way ANOVA).

Supplementary Figure 1

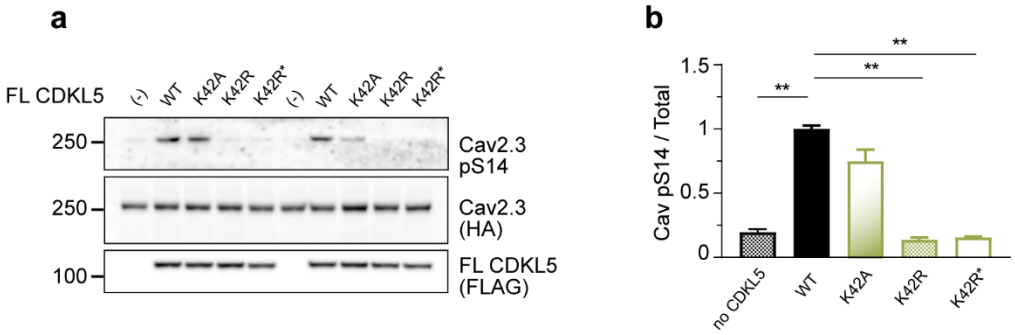

Supplementary Fig. 1: Full-length CDKL5 phosphorylates Cav2.3. a Western blot of HEK293 cells stably expressing human β3/α2δ1 subunits and transiently co-transfected with human WT HA- α1E (Cav2.3) and FLAG-CDKL5 full length (FL CDKL5: WT, K42A, K42R, K42R*+DFG-AFG kinase dead mutants). (-) transfection condition excludes CDKL5. The K42A mutation in FL-CDKL5 retains some kinase activity on α1E, while K42R and K42R* mutants are fully inactive and were thus selected for electrophysiology experiments. **b** Quantification of relative phospho-α1E (pS14 Cav2.3) levels for the experiment in **a** (**p<0.0001, Brown-Forsythe & Welch ANOVA, Dunnet's test; n=4-6, 3 blots, 2 transfections).

Supplementary Figure 2

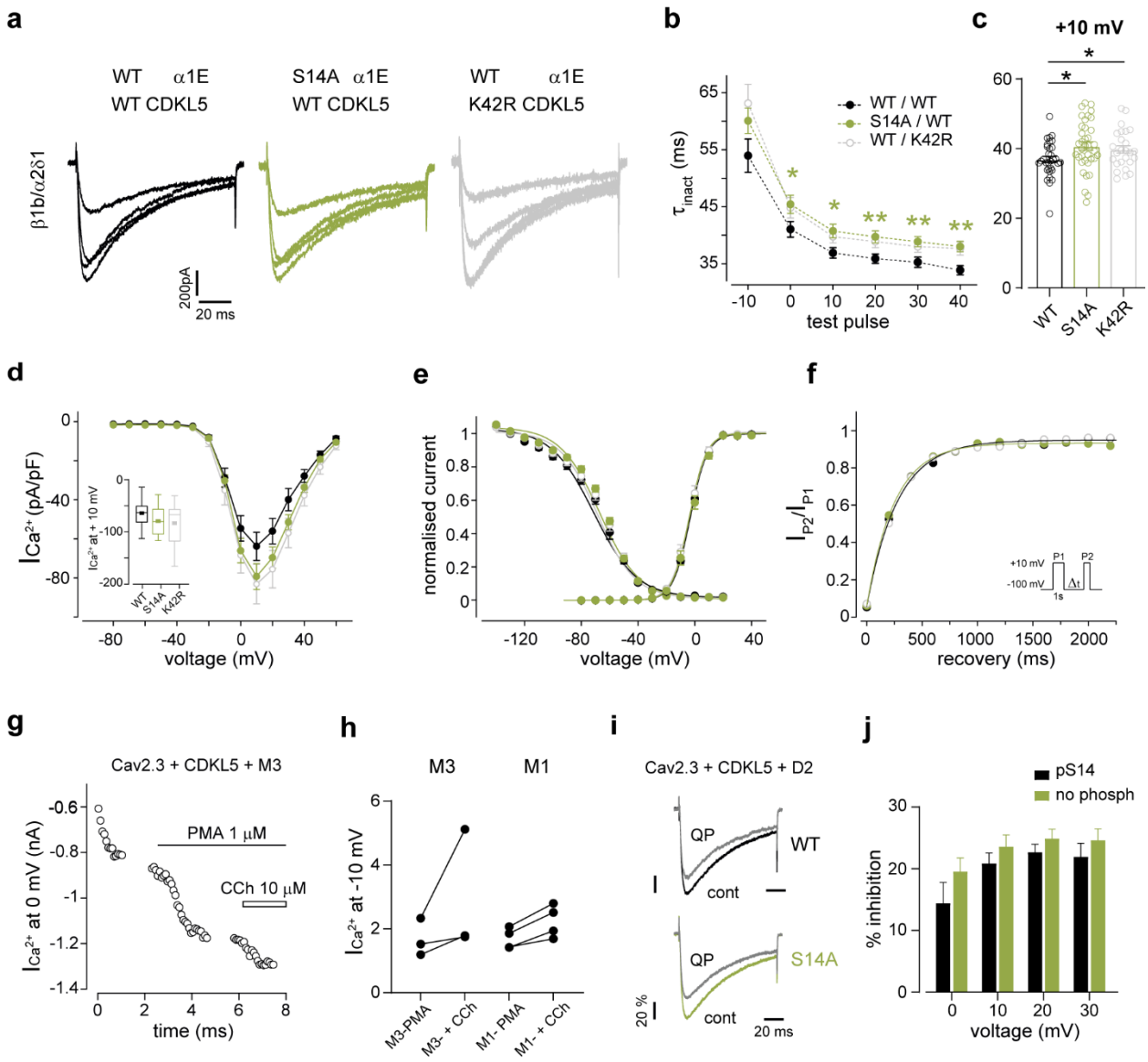

Supplementary Fig. 2: Functional characterization of phospho-Ser14 Cav2.3 in HEK 293 cells expressing β1 accessory subunit. a Depolarization-evoked current responses in HEK293 cells stably expressing human β1/α2δ1 subunits and co-transfected with human Cav2.3 (WT α1E or S14A α1E mutant) and FLAG-CDKL5 full length (WT CDKL5 or K42R*+DFG-AFG kinase dead CDKL5 mutant). Colours denote different construct combinations. Traces show steps from -10 to +20mV from -100mV; Ca^{2+} was charge carrier. **b** Open channel inactivation tau (τ_{inact}) for Cav2.3 with (WT/WT, n=28-32) and without (S14A/WT, n=34-37; WT/K45R, n=25-26) CDKL5 phosphorylation. WT/WT vs. S14A/WT:

1249 *p<0.05, **p<0.01 as indicated; WT/WT vs. WT/K42R*, p<0.01 at +40mV, p<0.05 at -
1250 10,10,20,30mV, Two-Way ANOVA, Fisher's LSD. Some of the cells included in this plot co-
1251 expressed M3 receptors; this was *per se* not found to affect inactivation kinetics. **c** Individual
1252 data points for τ_{inact} at +10mV (WT vs. S14A *p=0.014, WT vs. K42R *p=0.0468 two-tailed
1253 unpaired t tests). **d** Current-voltage relationship for experiments in **a** (WT/WT, n=15; S14A/WT
1254 n=15-17; WT/K42R* n=12-15) and current density at +10mV (inset, p>0.05, OneWay
1255 ANOVA). Data was acquired with 100ms voltage steps from -100mV in +10mV increments
1256 every 10s. **e** Normalised Cav2.3 conductance and voltage dependence of inactivation for the
1257 same three transfection conditions. Activation $V_{1/2}$, n: WT/WT -3±1 mV, 14; S14A/WT -3±1
1258 mV,17; WT/K42R* -2±1 mV, 14; Inactivation $V_{1/2}$, n: WT/WT -66±2 mV,14; S14A/WT -63±1
1259 mV,14; WT/K42R* -65±2 mV,11 (p>0.05, One-Way ANOVA). For inactivation protocol see
1260 Methods. Solid lines are Boltzman fits to the average data. **f** Inactivation recovery time using
1261 a double pulse protocol with variable inter-pulse recovery time (inset). Recovery tau, n:
1262 WT/WT 265±21 ms, 4; S14A/WT 263±21 ms, 5; WT/K42R* 290±15 ms, 4, p>0.05 Kruskall-
1263 Wallis, Dunn's test). **g** Time course of Cav2.3 current amplitude at 0mV in the β1/α2δ1-stable
1264 cell line co-transfected with α1E WT, CDKL5 and muscarinic receptor type 3 (M3). PKC
1265 activation with PMA did not occlude CCh enhancing effect. **h** Relative change in current
1266 amplitude for same experiment as **g** with either M1 or M3 receptors. No muscarinic inhibition
1267 was observed. **i** Cav2.3 current at +10mV in β1/α2δ1 cell line co-transfected with α1E (WT or
1268 S14A), CDKL5 (WT) and dopamine receptor type 2 (D2). Quinpirole 100nM (QP) application
1269 resulted in reliable and reversible inhibition of WT and S14A currents. **j** Quinpirole inhibition of
1270 Cav2.3 with (n=7) or without pS14 (n=12-13) (p>0.05 Two-Way ANOVA, Fisher's LSD). Data
1271 for α1E S14A phosphomutant and K42R* CDKL5 conditions (no phosphorylation) were pooled
1272 together.

1273

Supplementary Figure 3

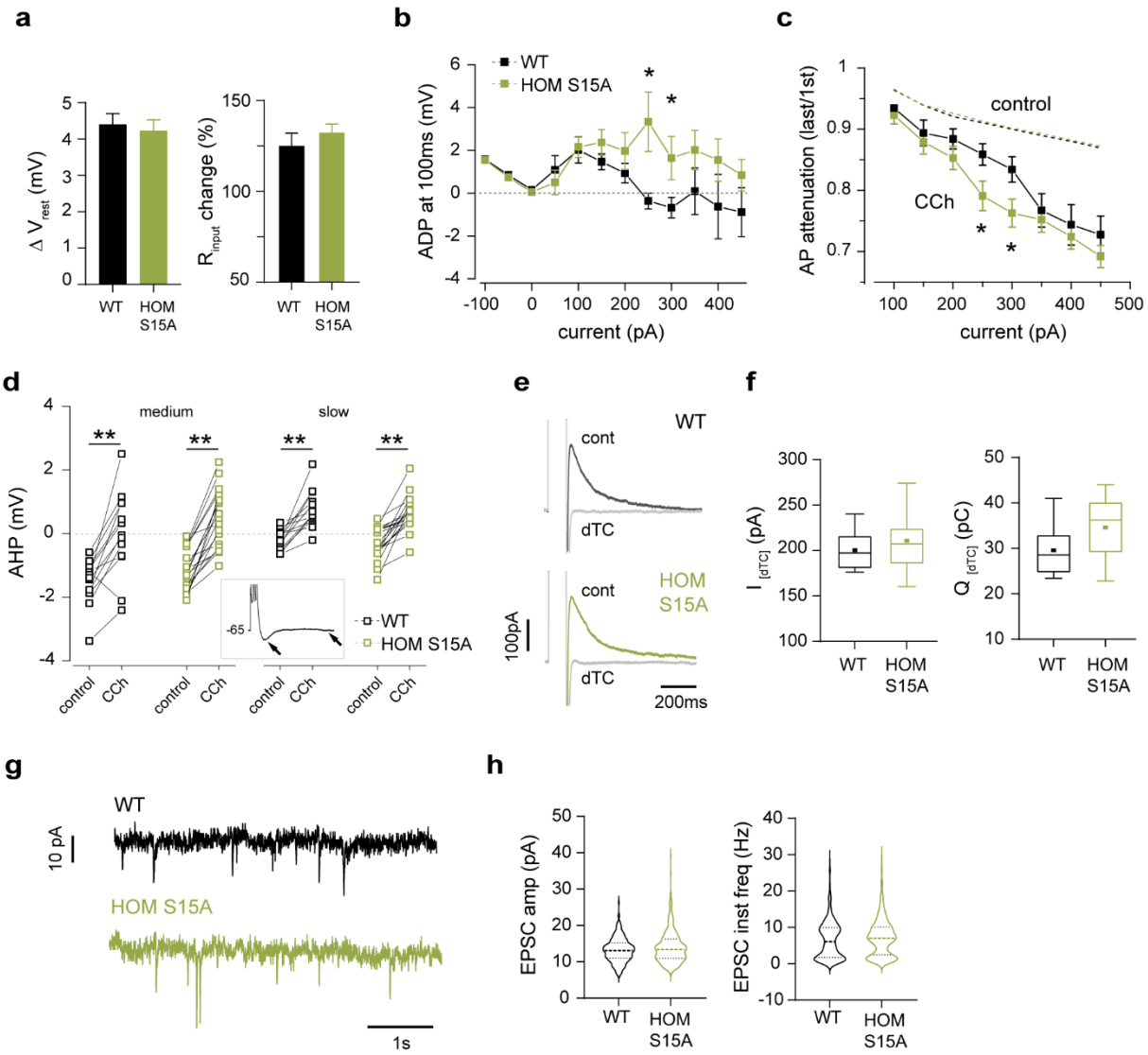

Supplementary Fig. 3: Additional CA1 neuron responses to carbachol and other intrinsic properties in adult WT and HOM S15A mice. a Relative changes in membrane potential (V_{rest}) and resistance (R_{input}) upon 10 μM CCh application in WT (13) and HOM S15A (17) neurons (7 mice/genotype, p>0.05, unpaired t tests). **b** CCh-evoked medium duration afterdepolarization (ADP) measured 100ms post 1s-long stimulus (WT n=13, HOM n=21; p=0.07 Two-way ANOVA; *p<0.05 Fisher's LSD). **c** Spike attenuation in control (dotted lines) and upon CCh-induced depolarization (markers) shown as ratio between last and first spike amplitude in 1s train (WT n=13, HOM n=19, Two-way ANOVA; *p<0.05 Fisher's LSD). **d** Medium and slow duration afterhyperpolarizations (AHPs) quantified at the peak and 500ms

1284 post stimulus, respectively (inset). AHPs evoked at -65mV by a 100Hz burst of somatic current
1285 injections were equal in WT (13) and HOM S15A (18-19) mice (mAHP, -1.5 *vs* -1.2mV; sAHP,
1286 -0.2 *vs* -0.3mV, p>0.05, unpaired t test). CCh suppression of burst-evoked AHPs (**p<0.01
1287 paired t tests) was unchanged between genotypes (mAHP ~Δ1.5mV, sAHP ~ Δ1mV, p>0.05
1288 unpaired t test). **e** Example traces of isolated small-conductance Ca^{2+}-activated SK currents
1289 and full inhibition by d-tubocurarine (dTC, grey). **f** dTC-sensitive current amplitude (left) and
1290 charge (right) for each genotype (WT n=8, HOM n=10 cells, 4 mice/genotype, p>0.05 unpaired
1291 t tests). **g** Example traces of spontaneous excitatory postsynaptic currents in WT and
1292 HOMS15A mice **h** Distribution of measured sEPSC properties for each genotype (WT: 1422-
1293 34 events, n=8 cells, HOM: 1455-65 events, n=7 cells; mean amp=14.0±0.8 *vs* 14.7±0.5 pA;
1294 instantaneous frequency=4.0±0.4 *vs* 4.3±0.3 Hz; N=3 mice/genotype; p>0.05, unpaired t
1295 tests).

Supplementary Figure 4

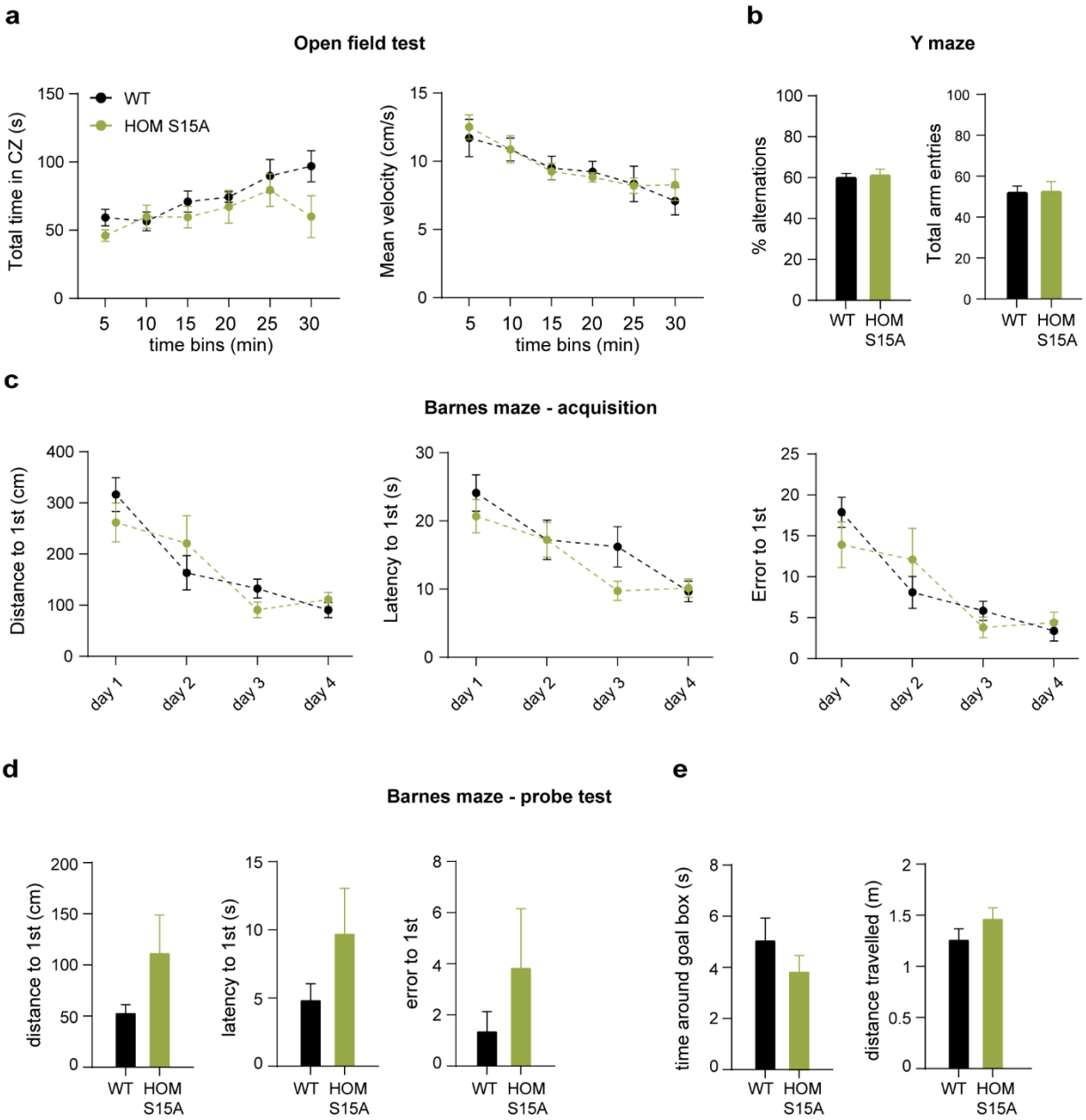

Supplementary Fig. 4: Behavioural characterization of Cav2.3 S15A phosphomutant mice. **a** left: total time in the central zone (CZ) of the open field arena in WT (N=8) and HomS15A (N=7) mice (30 min test) ($p>0.05$, Two-way Repeated Measures ANOVA; $p=0.08$ at 30 min, Fisher's LSD); right: mean displacement velocity ($p>0.05$, Two-way Repeated Measures ANOVA). **b** Percentage of successful spontaneous alternations (left) and total arm entries (right) in the Y-maze test show no deficits in arm recognition and exploration in

1303 phosphomutants ($p>0.05$, unpaired t test). **c** Acquisition phase of the Barnes maze test with
1304 improved performance for both groups in the first 4 training days: distance travelled (left),
1305 latency (middle) and number of errors committed (right) during the 1st visit to the escape box
1306 were not significantly different ($p>0.05$, Two-way Repeated measures ANOVA). **d** memory
1307 assessment on probe day 5 compared using the same parameters as in **c** ($p>0.05$, unpaired
1308 t tests). **e** Quantification of total time spent around the expected location of the goal box (left)
1309 and total distance travelled (right) ($p>0.05$ unpaired t tests).